Geology and Physical Properties Investigations by the InSight Lander

M. Golombek, M. Grott, G. Kargl, J. Andrade, J. Marshall, N. Warner, N. A. Teanby, V. Ansan, E. Hauber, J. Voigt, et al.

To cite this version :

Geology and Physical Properties Investigations by the InSight Lander

M. Golombek[1] · M. Grott[2] · G. Kargl[3] · J. Andrade[4] · J. Marshall[4] · N. Warner[5] ·
N.A. Teanby[6] · V. Ansan[7] · E. Hauber[2] · J. Voigt[2] · R. Lichtenheldt[8] ·
B. Knapmeyer-Endrun[9] · I.J. Daubar[1] · D. Kipp[1] · N. Muller[1] · P. Lognonné[10] ·
C. Schmelzbach[11] · D. Banfield[12] · A. Trebi-Ollennu[1] · J. Maki[1] · S. Kedar[1] ·
D. Mimoun[13] · N. Murdoch[13] · S. Piqueux[1] · P. Delage[14] · W.T. Pike[15] ·
C. Charalambous[15] · R. Lorenz[16] · L. Fayon[10] · A. Lucas[10] · S. Rodriguez[10] ·
P. Morgan[17] · A. Spiga[18,19] · M. Panning[1] · T. Spohn[2] · S. Smrekar[1] · T. Gudkova[20] ·
R. Garcia[13] · D. Giardini[11] · U. Christensen[9] · T. Nicollier[11] · D. Sollberger[11] ·
J. Robertsson[11] · K. Ali[1] · B. Kenda[10] · W.B. Banerdt[1]

Abstract Although not the prime focus of the InSight mission, the near-surface geology and physical properties investigations provide critical information for both placing the instruments (seismometer and heat flow probe with mole) on the surface and for understanding the

✉ M. Golombek
mgolombek@jpl.nasa.gov

[1]   Jet Propulsion Laboratory, California Institute of Technology, Pasadena, CA 91109, USA

[2]   DLR, Institute of Planetary Research, Berlin, Germany

[3]   Space Research Institute, Austrian Academy of Sciences, Graz, Austria

[4]   Mechanical and Civil Engineering, California Institute of Technology, Pasadena, CA, USA

[5]   SUNY Geneseo, Geneseo, NY, USA

[6]   School of Earth Sciences, University of Bristol, Wills Memorial Building, Queens Road, Bristol, BS8 1RJ, UK

[7]   Laboratoire de Planétologie et Géodynamique, CNRS URM6112, Université de Nantes, Nantes, France

[8]   DLR, Institute of System Dynamics and Control, Oberpfaffenhofen, Germany

[9]   Max Planck Institute for Solar System Research, Göttingen, Germany

[10] Institut de Physique du Globe de Paris, Paris, France

[11] ETH Swiss Federal Institute of Technology, Zurich, Switzerland

[12] Cornell Center for Astrophysics and Planetary Science, Cornell University, 420 Space Sciences, Ithaca, NY, 14853, USA

[13] Institut Supérieur de l'Aéronautique et de l'Espace (ISAE-SUPAERO), Université de Toulouse, 31400 Toulouse, France

nature of the shallow subsurface and its effect on recorded seismic waves. Two color cameras on the lander will obtain multiple stereo images of the surface and its interaction with the spacecraft. Images will be used to identify the geologic materials and features present, quantify their areal coverage, help determine the basic geologic evolution of the area, and provide ground truth for orbital remote sensing data. A radiometer will measure the hourly temperature of the surface in two spots, which will determine the thermal inertia of the surface materials present and their particle size and/or cohesion. Continuous measurements of wind speed and direction offer a unique opportunity to correlate dust devils and high winds with eolian changes imaged at the surface and to determine the threshold friction wind stress for grain motion on Mars. During the first two weeks after landing, these investigations will support the selection of instrument placement locations that are relatively smooth, flat, free of small rocks and load bearing. Soil mechanics parameters and elastic properties of near surface materials will be determined from mole penetration and thermal conductivity measurements from the surface to 3–5 m depth, the measurement of seismic waves during mole hammering, passive monitoring of seismic waves, and experiments with the arm and scoop of the lander (indentations, scraping and trenching). These investigations will determine and test the presence and mechanical properties of the expected 3–17 m thick fragmented regolith (and underlying fractured material) built up by impact and eolian processes on top of Hesperian lava flows and determine its seismic properties for the seismic investigation of Mars' interior.

Keywords InSight · Mars · Geology · Physical properties · Surface materials

1 Introduction

The InSight (**In**terior Exploration using **S**eismic **I**nvestigations, **G**eodesy and **H**eat **T**ransport) mission is a Discovery Program lander to investigate the internal structure of Mars and the differentiation of the terrestrial planets (Banerdt et al. 2018). The spacecraft carries a seismometer (SEIS, Lognonné et al. 2018) with a Wind and Thermal Shield (WTS), heat flow probe (Heat Flow and Physical Properties Package, HP³, Spohn et al. 2018) and a precision tracking system (Rotation and Interior Structure Experiment, RISE, Folkner et al. 2018) to measure the size and state of the core, mantle and crust. The lander is designed to operate on the surface for one Mars year after landing (November 2018), listening for marsquakes and impacts, measuring heat flow (including the sub-surface and surface temperature), and tracking the precession and nutation of the spin axis. The spacecraft is based on the Phoenix (PHX) lander and consists of a cruise stage, aeroshell, and backshell. It will land on smooth plains below −2.5 km elevation (for entry, descent and landing)

[14] École des Ponts Paris Tech, Paris, France

[15] Imperial College, London, UK

[16] Applied Physics Lab, Johns Hopkins University, Baltimore, MD, USA

[17] Colorado School of Mines, Golden, CO, USA

[18] Laboratoire de Météorologie Dynamique (LMD/IPSL), Sorbonne Université, Centre National de la Recherche Scientifique, École Normale Supérieure, École Polytechnique, Paris, France

[19] Institut Universitaire de France, Paris, France

[20] Schmidt Institute of Physics of the Earth, Moscow, Russia

and between 3–5 °N latitude (for solar power and thermal management) in western Elysium Planitia, which also satisfies other engineering and instrument deployment constraints (Golombek et al. 2017).

The spacecraft also carries a meteorology package, a magnetometer (Banfield et al. 2018), two color cameras to image the surface (Maki et al. 2018), and an arm to deploy the instruments onto the surface (Trebi-Ollennu et al. 2018), that together allow investigations of the atmosphere, surface geology, and physical properties of surface materials. The geology investigation on InSight is considered ancillary science that does not interfere with the main science requirements or objectives of the mission. Although determination of physical properties of surface materials during penetration of the heat flow probe or mole into the subsurface and the derivation of thermal inertia by the surface radiometer is part of the HP^3 instrument investigation (Spohn et al. 2018), the physical properties of surface materials will also be studied by SEIS, both passively (e.g., Knapmeyer-Endrun et al. 2017) and actively during HP^3 hammering (Kedar et al. 2017), and via interactions of the scoop at the end of the arm with the surface. Both the geology and physical properties investigations are relevant to deploying the instruments on the surface and interpreting the waveforms detected by SEIS. As a result, both investigations provide important information that supports the main science objectives of the mission. The geology and physical properties investigations are being developed and operated during the mission by two science theme groups, the Geology and Near Surface Properties theme groups; the change detection portion of geology (eolian activity) is being coordinated with the Atmospheres theme group.

The goal of this paper is to describe in one location, the geology and physical properties investigations planned by the InSight mission. Measurement of the physical properties by SEIS and HP^3 are described in the corresponding instrument papers and referenced and summarized herein, but this paper additionally includes contributions from the arm and scoop and explores the synergy between all of the measurements. Investigation of the geology of the landing site makes use of images acquired by the color cameras and the definition of surface materials and terrains observed in them as well as their physical properties. This paper begins with a brief description of the instruments and Instrument Deployment Arm (IDA) that are relevant to the geology and physical properties investigations. Next the landing site in Elysium Planitia and its geologic setting are briefly described to frame the surface observations to be made by the lander. The geology investigation is described, including meteorology observations and their relation to eolian activity (motion of sand, granules and smaller grains, migration of bedforms, and dust devil tracks) and the relevance to the selection of the locations on the surface to place the instruments. The description of the physical properties investigation includes the contributions from HP^3, SEIS (both passive and active), and the IDA and includes a description of sophisticated mechanical models that will help interpret the granular interactions during mole penetration and contact of the scoop with surface soils. Finally, results from the geology and physical properties investigations can be compared with predictions from remote sensing data and modeling investigations carried out during the landing site selection process (Golombek et al. 2017).

2 Instruments and Spacecraft Systems Relevant to Geology and Physical Properties

2.1 IDA

The InSight Instrument Deployment System (IDS) is comprised of the Instrument Deployment Arm (IDA), scoop, five finger "claw" grapple to pick up the instruments, arm-mounted
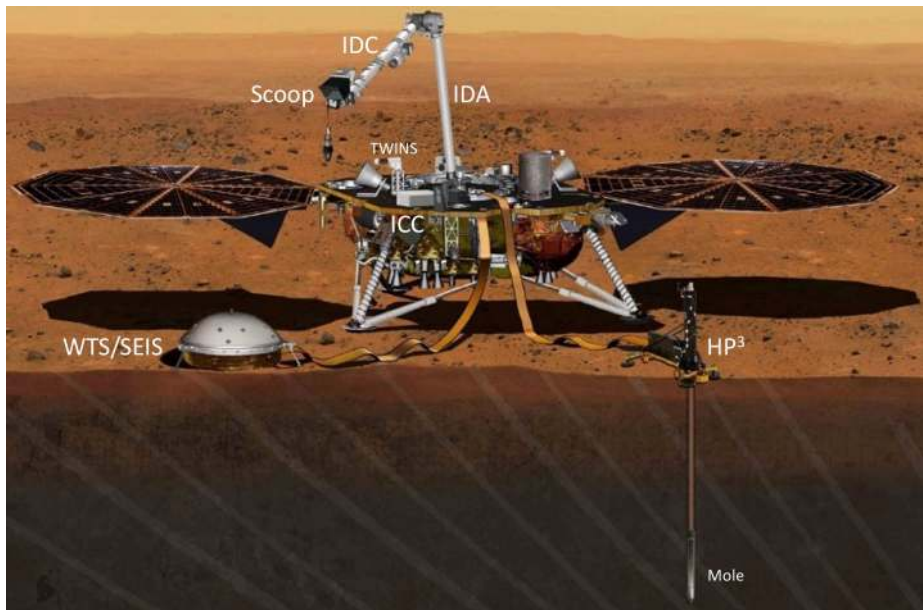
Fig. 1 Perspective view of the InSight lander with instruments and the arm (IDA) labeled. The IDC is mounted near the IDA elbow and looks down the arm towards the scoop. The ICC is mounted on the lander beneath the deck. The SEIS/WTS and HP^3 and mole are deployed in the workspace with tethers extending to the lander. One of the two TWINS booms for measuring wind speed and direction is labeled. The grapple is shown in the unstowed state, hanging from the arm, in much of the field of view of the IDC. Science imaging will occur with the grapple in the stowed configuration, attached to the IDA forearm. The lander controls its azimuth during landing so the workspace and instruments are to the south. The radiometer is mounted under the deck on the spacecraft on the opposite side, so the two radiometer surface spots are to the north of the lander

Instrument Deployment Camera (IDC), and the lander-mounted Instrument Context Camera (ICC) (Trebi-Ollennu et al. 2018) (Fig. 1). The IDA is a four degree of freedom back-hoe design manipulator with a 1.8-m reach and a scoop that can exert up to ∼80 N force. The IDA is used to point the IDC to take images of the surface, lander (selfie), lander elements, samples in the scoop, 360° panorama of the landing site, and the workspace in which the arm can place the instruments. IDC images allow visual confirmation of deployment steps, as well as acquisition of stereo image pairs used to create digital elevation models (DEM) and instrument deployment products of the workspace (Maki et al. 2018). The ICC is a single fish eye camera mounted underneath the lander deck (in a fixed location) and provides redundant context images of the workspace and horizon. The scoop consists of a single chamber with a front blade and a secondary blade on the bottom side. The scoop's front and secondary blades could be used to excavate materials (digging or scraping) and collect materials excavated in the workspace (piling). The use of the scoop would enable indentation, scraping, trenching, and trench cave-in experiments to infer mechanical properties of the martian soil at the landing site (Sect. 5). Because the primary function of the IDA is deployment of the instruments, use of the arm for soil mechanics experiments will depend on the health of the IDA after the instruments have been deployed and the availability of project resources. Nevertheless, for completeness potential scoop-based experiments that could be performed by InSight are described herein, with the understanding that they may or may not actually occur.

2.2 Cameras

The Insight lander is equipped with two cameras (Maki et al. 2018): an Instrument Deployment Camera (IDC) mounted on the lander robotic arm and an Instrument Context Camera (ICC) hard-mounted beneath the lander deck (see Fig. 1). Both cameras are flight spare units inherited from the Mars Science Laboratory Mission (MSL) mission (Maki et al. 2012): the IDC is a spare MSL Navcam and the ICC is a spare MSL Hazcam, both of which are inherited designs from the Mars Exploration Rover (MER) cameras with the same names (Maki et al. 2003). Both cameras have been upgraded from monochrome to color by replacing the monochrome detectors with Bayer color filter array detectors. The red, green, and blue bandpasses are the same for both cameras and are centered at wavelengths of approximately 450, 550, and 620 nm, respectively, which enables distinguishing between gray basaltic material and bright red dust (Maki et al. 1999). The ICC is permanently pointed towards the deployment workspace, nominally located to the south of the lander, and the IDC pointing is controlled by the motion of the robotic arm. Stereo IDC images are acquired by moving the IDC between image pairs (Abarca et al. 2018), and multi-image IDC panoramas can be acquired by pointing the camera around in a 360° fashion. A calibration target on the lander decks allows verification of the IDC radiometric performance, camera focus, and image scale (Maki et al. 2018).

2.3 HP^3

The Heat Flow and Physical Properties Package (HP^3) is comprised of a self-hammering probe called the HP^3 mole, which will hammer itself into the Martian regolith to a target depth of 5 m (Spohn et al. 2018). During the descent, HP^3 will stop at depth intervals of 50 cm to conduct thermal conductivity measurements, creating a depth profile of thermophysical properties. At each step, average thermal conductivity in the vicinity of the mole will be determined, and the first measurement will be at 30–70 cm below the surface (Grott et al. 2007; Grott 2009). In addition, the penetration speed of the probe depends on soil parameters including bulk density, compaction, cohesion, and internal friction angle, and mole progress can be analyzed using numerical models (Hansen-Goos et al. 2014; Lichtenheldt et al. 2014; Lichtenheldt and Krömer 2016; Kömle et al. 2015; Poganski et al. 2017a) as well as laboratory experiments of mole-soil interaction (Marshall et al. 2017), which can be used to constrain the mechanical properties of the Martian soil (see Sect. 5).

In addition to the thermal conductivity measurements carried out by the HP^3 mole, HP^3 has an infrared radiometer mounted under the lander deck on the spacecraft to measure the surface brightness temperatures in two fields of view facing north (opposite of the workspace). These measurements will determine the thermal inertia of surface materials, which can be related to regolith grain size and/or cohesion (Kieffer 2013; Presley and Christensen 1997a, 1997b; Presley and Craddock 2006; Piqueux and Christensen 2009). Stereo images of the radiometer spots will allow separation of the rocky and fine components (Fergason et al. 2006; Putzig and Mellon 2007; Vasavada et al. 2017; Hamm et al. 2018). Surface brightness temperature changes measured during partial eclipses of the sun for short periods of time by Phobos and Deimos are sensitive to material properties at shallower depths. Observations during the life of the mission will record the rate at which dust resettles at the landing site after being dispersed by the retrorockets during landing (Daubar et al. 2015, also see Sect. 4.7).

2.4 SEIS

The SEIS experiment consists of a 3-axis very broad band (VBB) and a 3-axis short period (SP) seismometer (Lognonné et al. 2018) that will be deployed on the surface on a tripod leveling system. The regolith's physical properties will influence SEIS measurements at the highest frequencies (100 Hz maximum sampling frequency and 50 Hz maximum resolvable frequency) due to resonances and waves within the regolith layer, as the seismic wavelengths are comparable to the expected regolith thickness. In addition, the VBB records not only the ground velocity, but also the ground tilt with very high sensitivity, which also depends on the near-surface elastic properties.

At high frequencies, passive SEIS monitoring can constrain near-surface structure through micro-seismic noise in the 1–30 Hz frequency band. This noise is mostly composed of high-frequency surface waves trapped in the upper layers of the regolith, due to the low seismic velocities of these layers (Withers et al. 1996; Delage et al. 2017; Knapmeyer-Endrun et al. 2017, 2018), which can be used to determine the shallow subsurface structure (Sect. 5.4.1). The high frequency signals also include the transfer function of the leveling system itself when deployed on the ground (Fayon et al. 2018). As described in Sect. 5.4.2, the horizontal transfer functions show resonances, and the frequencies at which these occur are related to the elastic properties and stiffness at the 3 contact points between the SEIS leveling system and the ground.

At low frequencies, ground tilt is expected to vary due to a number of sources, such as the thermal tilt of the subsurface (see Clinton et al. 2017, 2018 for time domain simulations), static loading of the lander in response to wind dynamic pressure (Murdoch et al. 2017a), and static loading caused by atmospheric pressure fluctuations due to planetary boundary layer activity (Murdoch et al. 2017b), including those associated with dust devils (Lorenz et al. 2015; Kenda et al. 2017). All of these sources generate significant seismic noise (Mimoun et al. 2017), that can also be treated as signal and processed together with the pressure data to provide a profile of the subsurface shear modulus (Sect. 5.4.1), after correcting for tilting due thermal variations. These time-varying signals can reach ± 30 µrad of tilt. Correcting this daily drift, a resolution of a few nrad in ground tilt in the 100–1000 s periods range may be achieved. The VBBs' acceleration might therefore also be used for active experiments with IDA, aiming to generate ground tilt in excess of these levels (Sect. 5.6.4).

2.5 HP³—SEIS Hammering Investigation

The hammering of the HP³ mole into the ground to 5 m depth to measure a vertical thermal conductivity profile will generate seismic signals that provide a unique opportunity to investigate the shallow martian subsurface (meters to possibly few tens of meters) using seismic-exploration techniques (Kedar et al. 2017). It is expected that the mole will require several thousand strikes to reach 3–5 m depth and each strike will generate a seismic signal. An adapted seismic-data sampling strategy to increase the recorded frequency bandwidth (e.g., Lognonné et al. 2018) will enhance the data analysis such that the signals can be used in a manner similar to high-resolution active-seismic experiments conducted with sledge-hammers for terrestrial engineering and environmental applications (e.g., Schmelzbach et al. 2005). The near-surface elastic properties can be derived from measurements of P- and S-wave velocities and attenuation, Q, and will be used to reduce travel-time and amplitude errors of globally propagating seismic waves as well as help test hypotheses on the shallow structure of the landing site.

2.6 Meteorology Instruments

InSight is equipped with a high precision pressure sensor, two booms to measure air temperature and wind, and a magnetometer (Banfield et al. 2018). While the primary use for the pressure sensor is to remove the influence of passing atmospheric pressure variations from the seismic signals (e.g., Murdoch et al. 2017a, 2017b), it will also prove useful in identifying nearby passage of dust devils (which may be confirmed by other sensors on InSight, e.g., Kenda et al. 2017, or from orbital images). The Temperature and Winds for InSight (TWINS) pair of booms (MSL heritage) will measure winds (Gomez-Elvira et al. 2012). The wind sensors, which are large finger-like probes with 3 wind sensing elements around their tips, are positioned at either edge of the spacecraft deck, whose data can be combined to yield the three-dimensional wind impinging on them.

The fact that both the pressure and TWINS sensors will be sampled continuously throughout the mission lifetime represents a unique capability that InSight offers surpassing previous landed Mars missions. Because there will be no gaps in the meteorological coverage (as there have been for all previous landers, e.g., Chamberlain et al. 1976; Seiff et al. 1997; Taylor et al. 2008; Gomez-Elvira et al. 2012), InSight will be able to conclusively quantify the peak winds occurring during an interval in which eolian change is observed. In addition, measurement of wind speed and direction offers the ability to determine the threshold friction wind stress for grain motion on Mars.

3 InSight Landing Site

3.1 Remote Sensing Properties

InSight will land in western Elysium Planitia located at ∼4.5 °N, ∼135.9 °E on Mars (Fig. 2). Selection of the landing site took approximately five years and included defining the engineering requirements for safe landing and deploying the instruments, mapping those requirements onto Mars using remote sensing data, and evaluating the surface characteristics in targeted orbital observations (Golombek et al. 2017). Analysis of remote sensing data during landing site evaluation and selection provides substantial insight to the characteristics of the surface and subsurface properties (Golombek et al. 2017).

The bulk thermal inertia, or the resistance to a change in temperature of the surface, and the albedo of the InSight landing site surface, are similar to the two Viking, MSL and Spirit landing sites. The Thermal Emission Spectrometer (TES) thermal inertia (Mellon et al. 2000; Putzig and Mellon 2007) of the InSight landing site ($\sim 200 \ \mathrm{J\,m^{-2}\,K^{-1}\,s^{-1/2}}$) is consistent with a surface composed of cohesionless sand size particles or a mixture of slightly cohesive soils, some rocks and thermally thin coatings of dust (e.g., Golombek et al. 2008a). Thermal Emission Imaging System (THEMIS) thermal inertias of the landing site show high thermophysical homogeneity at the 100 m scale, with a median of $\sim 180 \ \mathrm{J\,m^{-2}\,K^{-1}\,s^{-1/2}}$ (Golombek et al. 2017), corresponding to cohesionless ∼170 μm, fine sand based on laboratory work and theoretical relationships (Presley and Christensen 1997a, 1997c; Piqueux and Christensen 2011). The lack of significant seasonal variations in thermal inertia suggest the same material exists down to a few tens of centimeters depth. Comparison with remote sensing properties of existing landing sites (Golombek et al. 2008a) suggests the soils at the InSight landing site have bulk densities of $\sim 1000–1600 \ \mathrm{kg\,m^{-3}}$, particle sizes of ∼0.25–0.06 mm (medium to very fine sand), cohesions of less than a few kPa, and angle of internal friction of 30–40 °. Albedo and dust cover index (Ruff and Christensen 2002) are similar
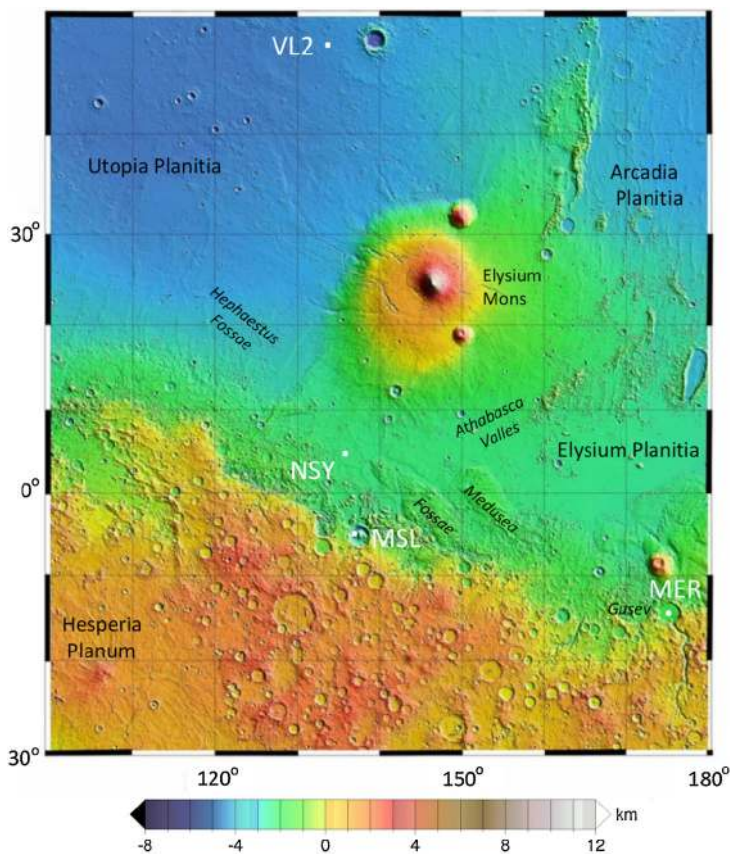
Fig. 2 Topographic map of the region around the InSight landing site (NSY) showing major physiographic features, mentioned in the text, as well as the Viking Lander 2 (VL2), Mars Science Laboratory (MSL) Curiosity, and Mars Exploration Rover (MER) Spirit landing sites. Spirit landed in Gusev crater and Curiosity landed in Gale crater. The map is a portion of the MOLA topographic map of Mars with elevations with respect to the geoid (Smith et al. 2001)

to dusty and low-rock abundance portions of the Gusev cratered plains, which have been dominantly shaped by impact and eolian processes (Golombek et al. 2006a).

Rock abundance at the landing site is very low and lies somewhere between that at the Phoenix landing site (2–4%) (Golombek et al. 2012b) and that at the Spirit landing site (∼5%) (Golombek et al. 2005, 2006a). Rock abundance is elevated around sparsely distributed rocky ejecta craters, which show high thermal inertia in THEMIS thermal images (Golombek et al. 2017). The InSight landing site is among the smoothest surfaces investigated for landing spacecraft on Mars as quantified at 1–5 m and 84 m length scale slopes in Context Camera (CTX) and High-Resolution Imaging Science Experiment (HiRISE) digital elevation models or DEMs (Fergason et al. 2017) as well as tuned photoclinometry (Beyer 2017). The surface is thus remarkably smooth and flat, except for common primary craters and secondary craters from the fresh, rayed crater Corinto, which is located ∼600 km north-northeast of the landing site. These secondaries in DEMs and photoclinometry slope maps show very shallow depth/diameter ratios (∼0.05) and interior slopes that rarely approach 15° (Golombek et al. 2017).

3.2 Geology from Orbit

3.2.1 Geologic Setting

Western Elysium Planitia lies just north of the global dichotomy boundary between elevated heavily cratered southern highlands and lower-standing, less cratered, northern plains (Figs. 1 and 2). The formation of the northern lowlands is the oldest geological event recognized on Mars, occurring in the pre-Noachian (Frey 2006), although younger tectonic and erosional processes have affected the dichotomy boundary since (McGill and Dimitriou 1990). The plains of western Elysium Planitia near the InSight ellipse are wedged between highlands to the south and west, a ridge of Medusae Fossae Formation to the east and southeast, Hesperian and Amazonian lavas from Elysium Mons to the north (Tanaka et al. 2014), and very young lavas from Cerberus Fossae and Athabasca Valles to the east (Vaucher et al. 2009).

The plains surface on which the InSight ellipse is located is mapped as an Early Hesperian transition unit (eHt) by Tanaka et al. (2014), which could be either sedimentary or volcanic. A volcanic interpretation of the plains is supported by: (1) the presence of rocks in the ejecta of fresh craters ∼0.5–2 km diameter arguing for a strong competent layer ∼5–200 m deep and weaker material above and below (e.g., Golombek et al. 2017; Warner et al. 2017; Catling et al. 2011, 2012); (2) exposures of strong, jointed bedrock overlain by ∼10 m of relatively fine-grained regolith in nearby Hephaestus Fossae in southern Utopia Planitia (Golombek et al. 2017; Warner et al. 2017); (3) mapping of volcanic flow fronts and vents in higher-resolution images described in the next section; (4) mafic mineral spectra of shallow exposed outcrops in fresh crater walls in CRISM data consistent with basalt flows (Pan and Quantin 2018); and (5) the presence of wrinkle ridges, which have been interpreted to be fault-propagation folds, in which slip on thrust faults at depth is accommodated by asymmetric folding in strong, but weakly bonded layered material ∼200–300 m thick (such as basalt flows) near the surface (e.g., Mueller and Golombek 2004; Golombek and Phillips 2010 and next section).

3.2.2 Geologic Mapping

The region around the InSight landing site was mapped from nadir visible images of Mars Express High Resolution Camera (HRSC) at 30 m/pixel combined with visible images acquired by Mars Reconnaissance Orbiter (MRO) CTX at 6 m/pixel (Figs. 3 and 4). The plains north of the landing site and in the northern and eastern edge of the ellipse are composed of lava flows, showing a wide diversity of textures from smooth, planar surfaces suggesting low viscosity lava (Fig. 3c, d and e) with possible inflation plateaus (Fig. 5), to rougher platy and ridged surfaces likely related to more viscous flows forming lobate lava fronts (Fig. 5g).

Lobate lava flow fronts in the northern part of the InSight ellipse, indicate that flows originated from near or around Elysium Mons. The lava flow-dominated terrains have been deformed by ∼5 km wide, ∼300 m high, wrinkle ridges generally less than tens of km long, (Watters 1988; Golombek et al. 1991; Schultz 2000; Mueller and Golombek 2004), which may have formed during the Late Hesperian global peak in wrinkle ridge formation on Mars (e.g., Mangold et al. 2000; Mangold et al. 2002; Head et al. 2002; Golombek and Phillips 2010). We re-designate these volcanic plains as the Hv plains unit (Hesperian volcanic unit) (Fig. 3b) based on direct observations of lava flow morphologies and the cumulative size frequency distribution of craters > 5 km in diameter. The N(5) value (cumulative number
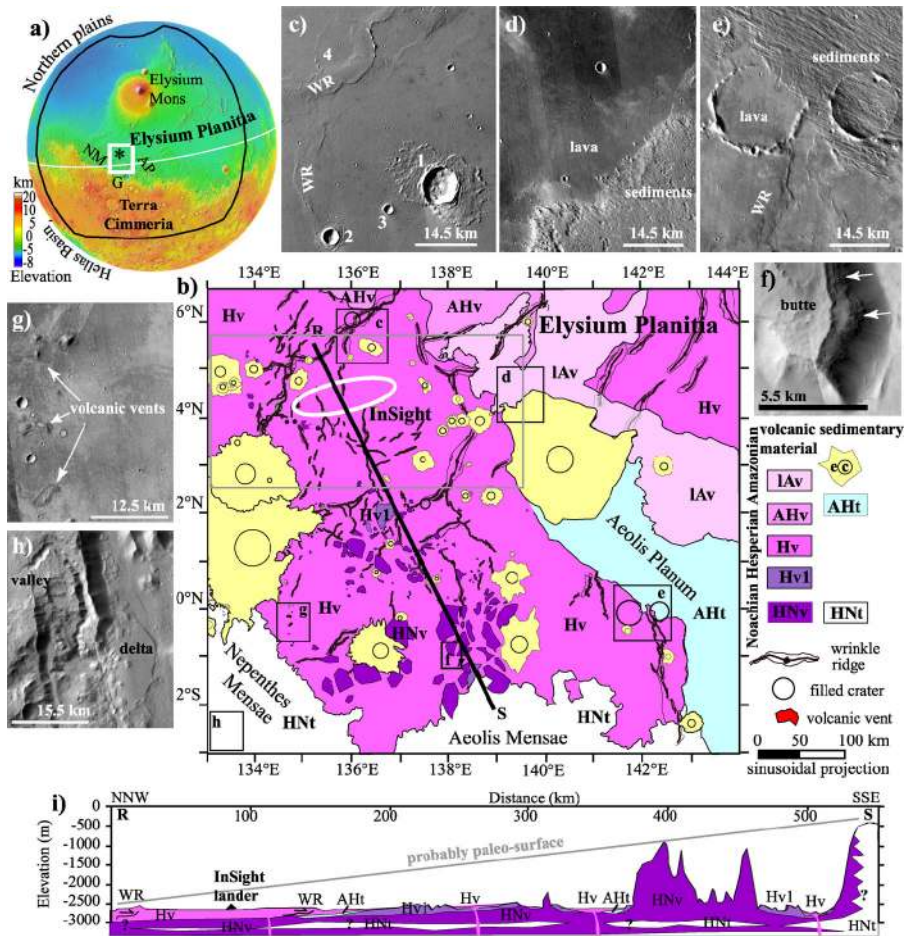
Fig. 3 Regional geologic map and supporting information. (**a**) MOLA topography centered on Elysium Planitia. Black box corresponds to location of Fig. 2. White box corresponds to the location of the regional geologic map (**b**) in which elevation ranges from 0 m to −3000 m. The star symbol (*) marks the InSight landing site. NM: Nepenthes Mensae. AP: Aeolis Planum. G: Gale crater. White line is the equator. (**b**) Regional geologic map. Colors and symbols of geologic units refer to Tanaka's nomenclature (N: Noachian > 3.7 Ga, H: Hesperian 3.7 to 3.1 Ga, and A: Amazonian < 3.1 Ga, l: late period, v: volcanic unit; t: transitional unit corresponding to unit located along the Martian dichotomy). Elysium Planitia is covered by volcanic material (pink color) with ages from the end of Noachian (HNv in remnant buttes) to Late Amazonian (lAv in the NE part of Elysium Planitia). Nepenthes Mensae and Aeolis Mensae are mainly composed of old surficial sedimentary material (Noachian to Hesperian, NHt) or younger volcano-sedimentary material (AHt), belonging to the Medusae Fossae Formation, respectively. Geologic structures include: fresh impact crater (**c**) and ejecta in yellow, wrinkle ridges, filled or partially filled impact craters, and volcanic vent. White ellipse corresponds to the InSight landing site. Grey box corresponds to the location of Fig. 4. Black boxes correspond to the location of insets: (**c**) HRSC image showing lava flows and craters (1, fresh impact crater and ejecta; 2 and 3 ejecta partially to totally covered by lava flows, respectively; 4, impact crater mostly filled by lava flow), WR: wrinkle ridges; (**d**) to (**h**): CTX images: (**d**) Amazonian lava flows (lAv) covering the cratered sedimentary material of Aeolis Planum; (**e**) Impact craters filled by lava flows (left) and the sedimentary material of Aeolis Planum (right); (**f**) Remnant 1300 m high butte showing dark layers probably composed of volcanic material; (**g**) Volcanic vents in southern part of western Elysium Planitia near Nepenthes Mensae; (**h**) large impact crater (Gale) incised by valleys terminating in fans in Nepenthes and Aeolis Mensae; (**i**) Geologic cross–section located along RS line on regional geologic map: stack of Hesperian lava flows materials overlying interbedded sedimentary and volcanic materials
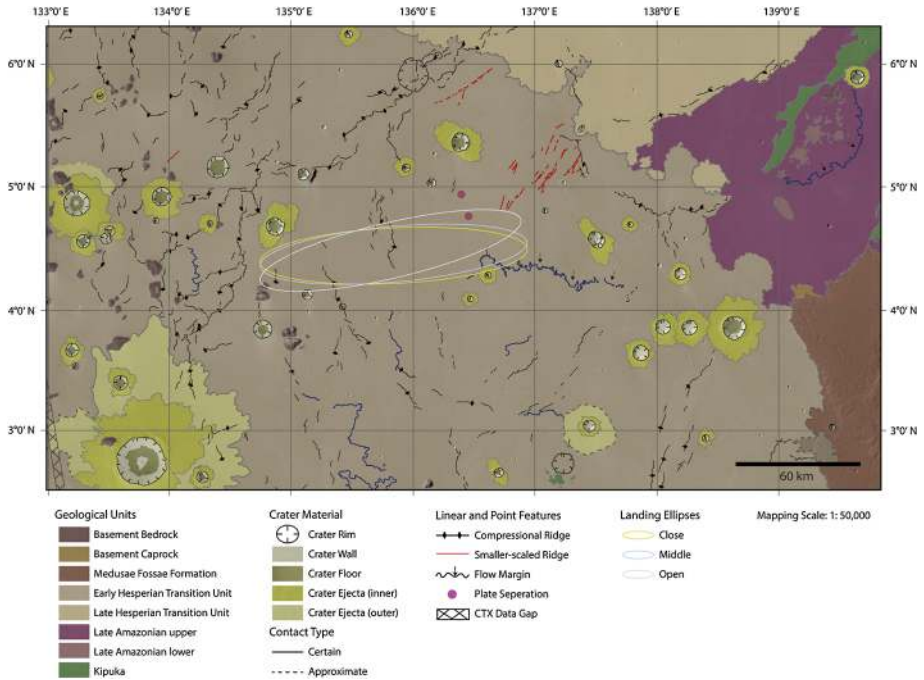
Fig. 4 Geological context map of the InSight landing site region on an HRSC-mosaic (with a pixel size of 25 m). CTX-images (6 m/pixel) were used to generate the geologic map at a digitizing scale of 1:50,000. White, blue and yellow are 130 km by 27 km ellipses for the open, middle, and close of the launch period

of craters with $D > 5$ km per 10^6 km^2) for this unit is 86 to 200, which corresponds to the Early and Late Hesperian (Werner and Tanaka 2011; Tanaka et al. 2014).

Within the majority of the landing ellipse and extending south to the planetary dichotomy, small, individual lava flow fronts are absent. However, the plains materials here exhibit wrinkle ridges, contain rocky ejecta craters, and embay remnant buttes of the southern highlands suggesting a similar lava flow origin. A more spatially-restricted crater count ($\sim 3.3 \times 10^3$ km^2) using CTX images was conducted over the landing ellipse (Warner et al. 2017). This count included all craters with $D > 200$ m and confirmed a Hesperian age from a cumulative fit to km-sized craters. However, a kink in the distribution exists for craters smaller than 2 km, suggesting resurfacing of 100-m-scale craters in the Early Amazonian. This suggests that plains materials in the InSight landing region were largely emplaced during the Hesperian, and that Amazonian-age resurfacing, likely related to volcanic activity, completely obliterated craters with maximum pristine depths of 200 m (assuming a depth to diameter ratio of ~ 0.2 for 1 km diameter craters, Pike 1974; Garvin et al. 2003; Watters et al. 2015). Partially filled craters north of the landing ellipse indicate that the volcanic infill is ~ 300 m thick (Fig. 3c and e). MOLA data suggest older Noachian craters are buried beneath the volcanic plains (Fig. 6). A geologic cross-section summarizes the spatial-temporal relationships between different units (Fig. 3i).

3.3 Terrains in the Landing Ellipse

The surficial characteristics of the landing ellipse were evaluated and mapped during landing site selection (Golombek et al. 2017) using co-registered MOLA, THEMIS (100 m/pixel),
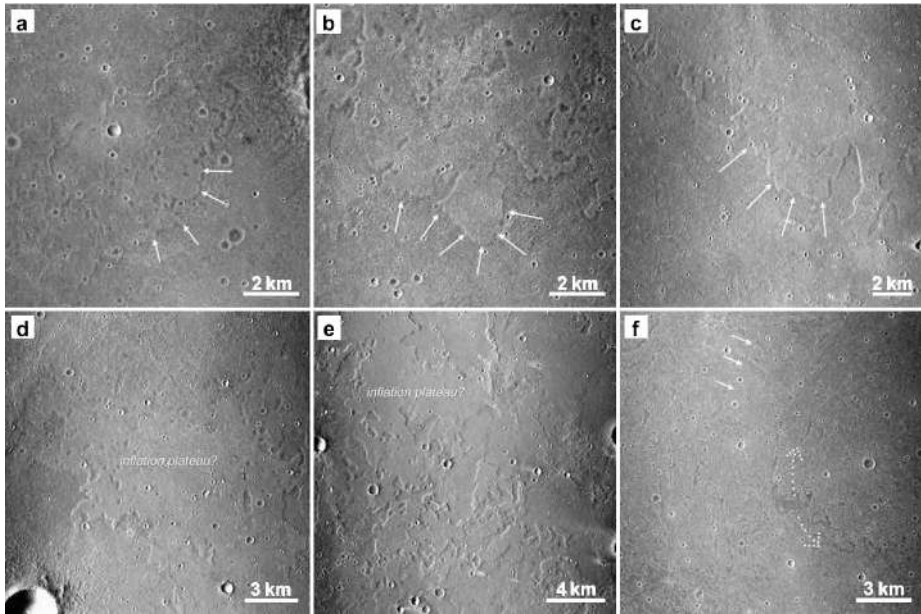
Fig. 5 Lava flow morphology at the InSight landing site. (**a**)–(**c**) Lobate flow fronts (arrows). The low aspect ratio of the flow fronts suggests an emplacement as sheet flows ((**a**): CTX D14_032660_1843; image center at ∼4.22 °N, 136.5 °E; (**b**): D15_033227_1841, ∼4.37 °N, 136.95 °E; (**c**): D04_028757_1855, 4.23 °N, 137.3 °E). (**d**), (**e**) Plateau-like flow units with flat surfaces, suggestive of lava inflation (Walker 1991; Hon et al. 1994; Bleacher et al. 2017) ((**d**): D04_028968_1853, 4.42 °N, 136.72 °E; (**e**): D04_028757_1855, 6.29 °N, 137.1 °E). (**f**) Platy flows, with shear fractures (white arrows) and relative motion indicated by dotted arrow (D14_032660_1843, 4.79 °N, 136.44 °E). North is up for all images

CTX (6 m/pixel), and HiRISE imagery (25 cm/pixel). A final terrain map (Fig. 7) was produced at a scale of 1:40,000 using a complete CTX mosaic, with confirmation of terrain types from HiRISE. The terrains were defined by their topographic characteristics, thermal properties (relative daytime and nighttime temperatures), albedo, rock abundance, and geomorphology. The terrain map displays surficial characteristics and variations that are relevant for landing and surface operations.

Visible light images, DEMs and photoclinometry reveal a constant moderate albedo, low relief and low regional and local slopes across the ellipse. The dominant terrain unit is termed "Smooth Terrain". THEMIS daytime and nighttime infrared mosaics (Christensen et al. 2004) indicate that Smooth Terrain is thermally uniform (Fig. 6a) and is composed of poorly consolidated sand that lacks rocks, with limited dust cover (Sect. 3.1). Variation in the thermal characteristics only occurs proximal to impact craters, where higher thermal inertia materials are indicated. CTX and HiRISE imagery reveal that abundant meter-sized rocks correspond with this high thermal inertia signature around craters ranging from 50 m to 2 km in diameter (Figs. 6a and 8). Eolian bedforms are also observed in the ejecta of fresh craters, trapped against rocks and crater rims. Bedforms and rocks are largely absent in the inter-crater regions, implying that rock and sand production, as well as recent sand mobilization and deposition, are limited to impact-proximal regions (Golombek et al. 2017, 2018; Sweeney et al. 2018). Dust devil tracks are ubiquitous across the region and suggest a dominant northwest to southeast wind direction (Fig. 8). The prevailing winds result in
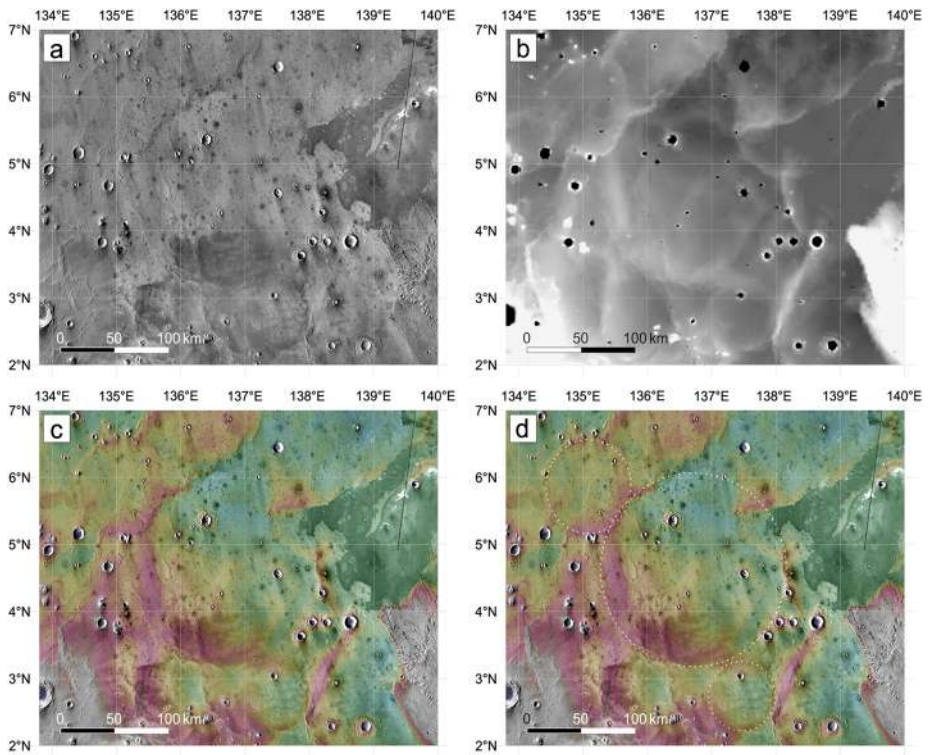
Fig. 6 Thermal and topographic maps of the InSight landing site region showing evidence for buried craters. (**a**) THEMIS-IR daytime image mosaic (Edwards et al. 2011). Note the dark impact craters with relatively cool daytime temperatures indicating they have higher thermal inertia and correspond to rocky ejecta craters. Note large craters are not rocky indicating they are ejecting weak material from below the 200–300 m thick lava flows. Dark unit to the east is made of very young volcanics from Athabasca Valles. (**b**) MOLA DEM emphasizing subtle topography of the volcanic plains. (**c**) Color-coded MOLA DEM overlaid on THEMIS-IR daytime image mosaic. (**d**) Same as c, with possible buried impact craters marked by dotted circles. Note how wrinkle ridges follow the rims of the craters

preferential bedform accumulation on the northwest exterior of crater rims and the formation of northeast-southwest trending bedforms on the floors of craters (Fig. 8).

Coupled with observations of wrinkle ridges and rocky ejecta craters, the Smooth Terrain surficial characteristics (Fig. 9) are consistent with a regolith that overlies a more competent bedrock unit (likely basaltic lava). Associated terrain types, identified during the landing site downselection mapping phase, further imply that the Smooth Terrain has a surficial regolith. The Etched and Gradational Etched terrain units occur outside of the ellipse (Fig. 7) and likely represent regions where the upper regolith was either completely or partially stripped of sand-size grains by eolian activity (Golombek et al. 2017). The open orientation of the landing ellipse also incorporates a localized terrain unit along its northeast margin called Ridged Terrain (Fig. 7). Ridged Terrain is defined by degraded lobate landforms that exhibit characteristic, lobate and ridged (i.e., compressional ridges in lava crust) lava flow morphology (Fig. 9). The local and regional slopes, thermal properties, albedo, and rock abundance of the Ridged Terrain are similar to the Smooth Terrain, implying some regolith cover.
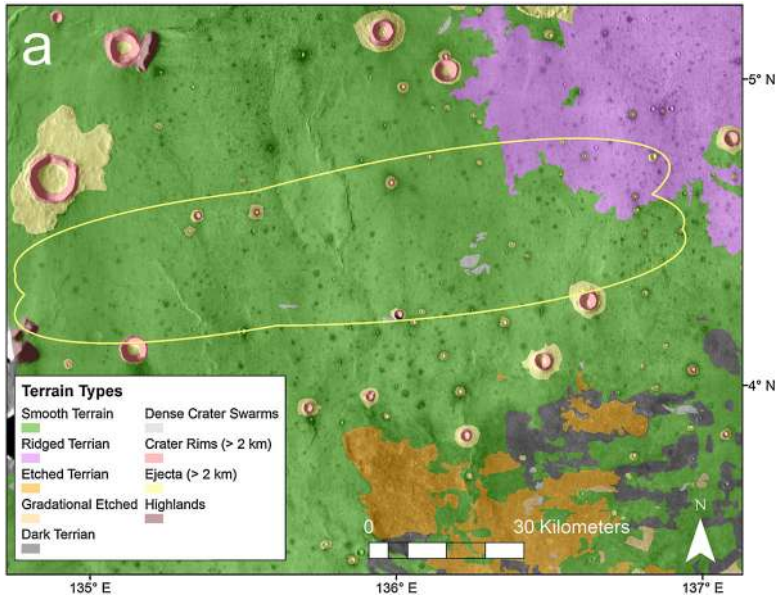
Fig. 7 Terrain map of the InSight landing region. The open, middle, and close orientations of the final landing ellipse (they rotate clockwise with launch date) were merged to display the possible range of landforms and surface terrains within the landing region. The dominant terrain types in the landing site include Smooth Terrain and Ridged Terrain. Crater Rims and Ejecta for craters > 2 km in diameter and Dense Crater Swarms (secondary crater clusters) are also present. Further information on the terrains can be found in Golombek et al. (2017)

Fig. 8 Example Rocky Ejecta Crater (REC) on Smooth Terrain in the landing ellipse. Meter to 10-meter-size rocks are identified by their shadows along the crater rim and within the continuous ejecta. Outside of the continuous ejecta in the Smooth Terrain (approximately 1 diameter from the rim) rocks are absent. Relatively bright eolian bedforms are present within the ejecta, trapped against the northwest rim of the crater, and on the floor of the crater. Dust devil tracks located to the northeast of the crater confirms a NW-SE dominant wind direction. HiRISE image ESP_035640
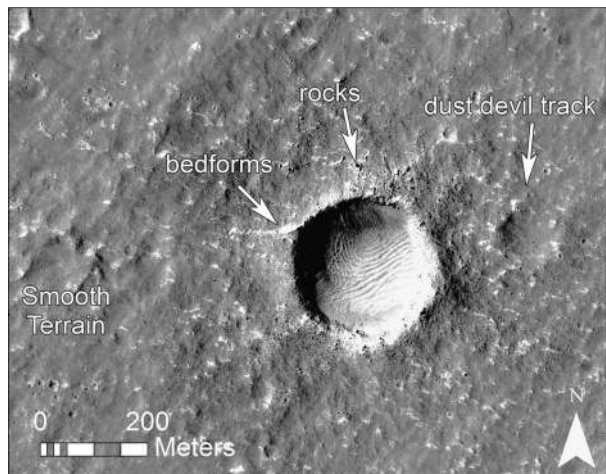
3.4 Rocky Ejecta Craters and Regolith Thickness

Rocky ejecta craters (RECs) in the landing ellipse indicate that a more competent rock-bearing unit occurs at depth. All craters in the landing ellipse between 200 m and 2 km in diameter exhibit meter-size rocks in their ejecta (Warner et al. 2017). However, many
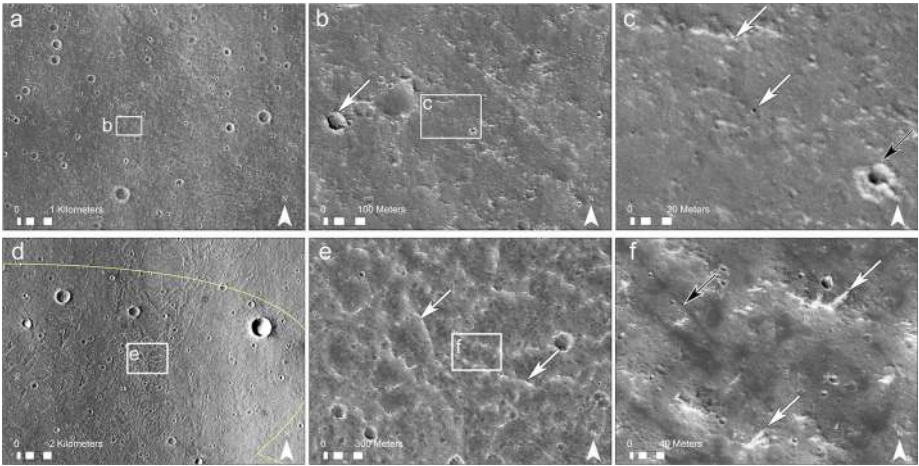
Fig. 9 Terrain samples from the InSight landing ellipse. (**a**) CTX image showing a typical example of Smooth Terrain. (**b**) HiRISE image sample of Smooth Terrain. The white arrow points to a relatively fresh, 50 m diameter REC. (**c**) Zoomed in portion of the Smooth Terrain showing one rock and bright bedforms (white arrows). Rocks and bedforms are rare on the intercrater plains. The black arrow is a secondary crater from Corinto with characteristic bright ejecta. (**d**) CTX image displaying the Ridged Terrain in the northeast corner of the ellipse (open orientation). Ridged terrain is identified by lobate landforms and sub-parallel ridges that are oriented parallel to the lobate margin. (**e**) HiRISE image of the ridged terrain. White arrows point to the crests of the sub-parallel ridges. These ridges are interpreted to represent compression ridges on the surfaces of lava flows (Theilig and Greeley 1986; Gregg 2017). (**f**) The ridges are elevated landforms that trap eolian bedforms (white arrows). Dust devil tracks are also common in the Ridged Terrain (black arrow)

craters below 200 m and most craters below 50 m in diameter, including fresh craters and young (< 2.5 Ma) secondaries from Corinto crater (Preblich et al. 2007; Bloom et al. 2014; Hundal et al. 2017) completely lack rocks. This suggests that smaller impacts did not excavate deep enough to access the rocky unit. The cumulative size-frequency distribution (SFD) of RECs in the ellipse confirms this observation and demonstrates a decrease in the frequency of RECs at diameters ≤ 200 m and a complete lack of RECs below 50 m (Warner et al. 2017). These observations support the hypothesis that the landing site is capped by a less competent, loosely-consolidated regolith, consistent with the terrain mapping.

Using established depth of excavation relationships ($d = 0.084D$ from Melosh 1989), and the minimum cut-off diameters for rocky ejecta around craters, Warner et al. (2017) determined that the landing ellipse is covered by a 3 to 17 m thick regolith. Concentric craters, identified in HiRISE images, further indicate a two-layer, near-surface stratigraphy that is consistent with a weaker regolith layer overlying competent rock (Fig. 10). The inner concentric craters form within the larger outer crater at depths between 2 and 5 m, measured relative to the surrounding plains. A surface regolith with relatively low density in western Elysium Planitia (Ojha et al. 2018) is also inferred from modeled gravity and topography data (Konopliv et al. 2011, 2016; Goossens et al. 2017) and comparisons to lunar impact generated regolith whose density increases with depth (Wieczorek et al. 2012).

A REC density map (diameter > 30 m), constructed using all HiRISE images in the landing ellipse, indicates a higher density grouping of fresh RECs (Class 1–3; see next section and Warner et al. 2017) along the strike of wrinkle ridges (Fig. 11). Although obvious secondary clusters and chains (noted for their alignment with other clusters and their uniform state of preservation), including those derived from Corinto crater to the north, were removed from the density analysis, it remains possible that the high density
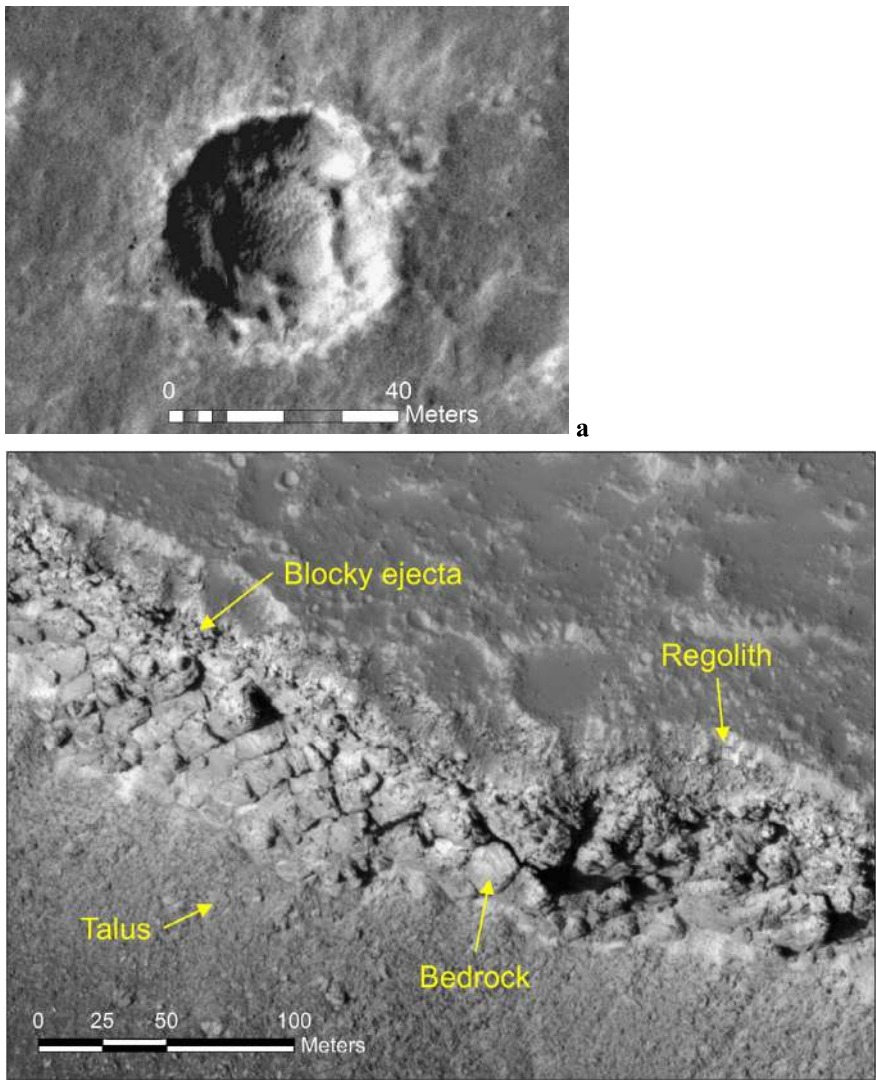
Fig. 10 (a) Concentric (nested) crater (HiRISE images) within the InSight landing ellipse. Most concentric craters are < 100 m in diameter and are typically less than < 50 m in diameter. This 40 m example exhibits low rock abundance in its continuous ejecta. The inner nested crater and the overall lack of rocks within the ejecta support the presence of a two-layer stratigraphy of a weak relatively fine-grained regolith that overlies a more competent rocky unit. (b) A portion of the exposed steep scarp of Hephaestus Fossae in southern Utopia Planitia at 21.9 °N, 122.0 °E showing ~10 m thick, relatively fine-grained regolith overlying blocky ejecta that grades into strong, jointed bedrock

of RECs is a function of non-random clustering in the crater population (Platz et al. 2013; Warner et al. 2015). To evaluate this possibility, all similarly fresh > 30 m diameter non-rocky craters were also mapped in all HiRISE images in the ellipse (Fig. 11). The density of RECs was normalized to account for possible spatial clustering by comparing the total number of rocky craters within 5 km grids to the total number of all fresh craters present

Fig. 11 Map of the distribution of fresh RECs (white dots) and fresh non-RECs (black dots) > 30 m diameter within the InSight landing site. Only the freshest Class 1 to 3 craters are included (see Warner et al. 2017 for classification description). (**a**) A grid (5-km-spacing) showing the ratio of fresh RECs relative to the total number of fresh craters. The black lines are traces of wrinkle ridges. A higher ratio of RECs occurs along and between the ridges in the central and west-central portion of the ellipse. A lower ratio of RECs relative to the total occurs further east and to the extreme west. (**b**) A grid (5-km-spacing) showing the ratio of fresh non-rocky craters to the total. The wrinkle ridges in the central and west-central portion of the ellipse generally corresponds with a lower ratio of > 30 m diameter, fresh non-rocky craters relative to the total number of fresh craters. Although local variability in regolith thickness is high (note close proximity of RECs and non-RECs), these relationships suggest a locally thin regolith in the west central portion of the ellipse
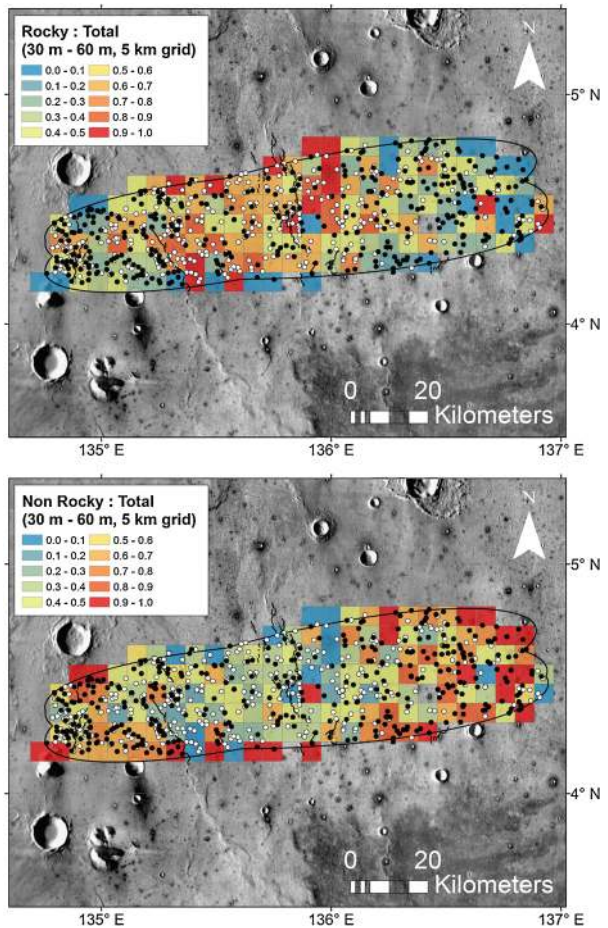
(rocky and non-rocky) in that same grid. The data confirms that there is a higher percentage of RECs relative to the total number of craters along the strike of the wrinkle ridges, as well as between wrinkle ridges in the west-central region of the ellipse. There, 60% to 90% of all fresh craters that are > 30 m in diameter exhibit rocks in their ejecta. However, the relative percentage of rocky craters to total craters generally decreases away from the ridge near the eastern and westernmost edges of the ellipse. At those locations, between 10% and 40% of all craters in this size range exhibit rocks in their ejecta. These data suggest regolith thickness variations across the landing site that may be caused by local slope variations and/or surface processes (e.g., wind) that locally may have stripped regolith proximal to wrinkle ridges (Warner et al. 2017).

3.5 Surface Processes and Rates

Craters in the InSight landing site degrade over time, like all martian craters do, through an overall reduction in rim height, shallowing of the interior and exterior rim slope, and infill by eolian materials. Golombek et al. (2017) and Warner et al. (2017) defined a 1 to 5 morphologic classification system for the RECs, relating crater interior, rim, and ejecta

characteristics (e.g., rock abundance) to relative age. Class 1 craters represent the most pristine, youngest RECs, while Class 5 represent the oldest craters to still preserve rocks in their ejecta. Using the size-frequency distribution of different class groupings, Warner et al. (2017) and Sweeney et al. (2016, 2018) show that ∼150 to 200 Myr separate each morphologic class. The age constraints, coupled with morphometric data gathered from HiRISE DEMs, indicate that craters predominately degrade through relatively slow diffusional slope processes (e.g., mass wasting, gravitational creep and eolian abrasion) at rates similar to other estimated erosion rates on Hesperian-age terrains on Mars (Sweeney et al. 2018), including Gusev crater (Spirit) (Golombek et al. 2006a, 2006b) and Chryse Planitia (Pathfinder) (Golombek and Bridges 2000). The measured reduction in rim height over measurement time intervals of ∼150 Myr and ∼500 Myr indicates extremely slow surface erosion rates relative to terrestrial and Noachian rates on Mars of ∼ 0.02 m Myr^{-1} and 0.002 m Myr^{-1}, respectively (see Golombek et al. 2014 for discussion). However, slope processes do not account for the total crater depth-related degradation, as a significant component of eolian infill is also observed.

Eolian bedforms occur almost exclusively on the floors and within the ejecta blankets of all RECs, suggesting that the impact process supplies the sand. Fragmentation theory supports the likelihood that ongoing comminution of bedrock to regolith by impact gardening can produce an abundance of sand-size material (Charalambous et al. 2017; Morgan et al. 2018; Golombek et al. 2018). Comparing the morphology of Class 1 to Class 5 craters, eolian materials organize into bedforms soon after crater formation and migrate over the rims and into the interiors of the craters, contributing to the total depth degradation. Through a comparison of crater topographic profiles from DEMs at different states of modification that are modeled through diffusional slope modification, ∼30% of the total measured depth-related degradation at the Insight landing site is related to eolian infill (Sweeney et al. 2018). Using the age constraints for the RECs, this provides an eolian infill rate of ∼ 0.008 m Myr^{-1}. Combined with rim erosion, the infill rate results in an overall crater degradation rate of 0.03 m Myr^{-1} and 0.01 m Myr^{-1} measured over 150 Myr and 500 Myr, respectively. These rates are so slow, that they argue for a surface dominated by impact and eolian processes since the lava flows were deposited (e.g., Golombek et al. 2006a, 2006b, 2014, 2017).

3.6 Fragmentation

Fragmentation theory developed by Charalambous (2015) shows that repeated fragmentation can be modeled by a negative binomial (NB). Using the observed rock distribution at the landing site, the theory was used to determine the abundance of 10 cm size rocks that could potentially stop the HP^3 mole (Golombek et al. 2017). The size-frequency distribution of impact craters and the age of the surface was used to define a maturity index to synthesize the particle size distribution of the regolith.

A compilation of rock counts from HiRISE images for the InSight, Phoenix and Spirit landing sites and surface rock counts from the later two was matched using fragmentation theory (Golombek et al. 2017). The model predicts that the rock population down to 5–10 cm is likely similar to that observed at the Spirit landing site (Columbia Memorial Station, CMS) (Golombek et al. 2006a, 2017). Subsequently, the model was extrapolated to smaller size particles (∼0.6 mm, coarse sand) (Morgan et al. 2018; Charalambous et al. 2017; Golombek et al. 2018) using microscopic image measurements of the size-frequency distribution of sand at the Spirit and Curiosity landing sites (McGlynn et al. 2011; Minitti et al. 2013; Ehlmann et al. 2018). This extrapolation indicates that sand at the InSight

landing site could have been produced by impact comminution and rounded by saltation (Golombek et al. 2018).

4 Surface Geology Investigation

4.1 Surface Geology

The surface geology investigation will characterize the geology of the InSight landing site and provide ground truth for orbital remote sensing data. Similar investigations for previous missions have established the basic geologic evolution of the local region, identified the geologic materials present, and quantified their areal coverage. By understanding the materials that surround the InSight lander, the site can be also be used as ground truth for orbital remote sensing data and thus aid in scientific analysis and future landing site selections (e.g., Golombek et al. 2008a).

4.2 Geologic Materials and Surfaces

The geological materials and surfaces present can be mapped in surface images by evaluating their texture, fabric and color. Surface images of all landing sites on Mars have thus been analyzed to determine the surficial geology, the geologic evolution of the area, and the processes responsible. Although rovers have a distinct advantage in understanding the geology by being able to traverse and inspect surface materials at disparate locations up close, even fixed landers (Viking Lander 1 and 2, Phoenix) or those with a small rover (Pathfinder) have performed successful surface geology investigations (e.g., Binder et al. 1977; Mutch et al. 1977; Golombek et al. 1997a, 1999a; Smith et al. 2009). These investigations characterized and mapped soil deposits, rocks and their distributions, and identified eolian bedforms, craters, and troughs (due to ice). They also placed the surfaces observed into orbital context and showed that materials and their properties observed by the landers could be related to orbital remote sensing observations (e.g., Christensen and Moore 1992; Golombek et al. 2008a).

The InSight geology investigation will be similar to those conducted by previous surface missions. Color images of the surface will be examined to distinguish different geologic materials such as soils, rocks, and bedrock. In addition, craters, eolian bedforms and any other geologic features observed will be mapped. Stereo images and full 360° panoramas along with images of the lander feet and area beneath the lander will be examined for alteration during landing. Thermal inertia of the radiometer spots will provide information about particle size and cohesion (Sect. 4.5). The areal extent of different materials will be measured along with the sizes of rocks within view of the lander. Rock morphology, morphometry and size-frequency distributions can be characterized and measured and related to their origin and emplacement (e.g., Garvin et al. 1981; Yingst et al. 2007, 2008, 2013; Craddock and Golombek 2016). All of these observations can be compared to expectations from orbital data and used to characterize the material present on Mars and improve future landing site selection (e.g., Christensen and Moore 1992; Golombek et al. 2008a).

4.3 Geologic Evolution and Subsurface Structure

The information gathered about the geology of the surface can be used to infer the geologic processes responsible and the geologic evolution of the surface. As examples, eolian bedforms and craters indicate saltation of sand size grains and impact, two processes that are

expected to have been active at the landing site as they have been observed in orbital images (e.g., Sect. 3). Rock texture and morphometry have been related to their origin and the mechanism of emplacement (Binder et al. 1977; Mutch et al. 1977; Yingst et al. 2007, 2008, 2013; Craddock and Golombek 2016; Szabo et al. 2015).

The shallow subsurface structure of the landing site was also a topic of intensive investigation during landing site selection (Golombek et al. 2017) and is clearly important for SEIS and HP^3 (Sect. 3). As a result, the geology of the surface and its evolution will be used to infer the subsurface structure. This will also depend on information gathered from the physical properties investigation (Sect. 5). Both of these investigations will be used to characterize the surface structure of the landing site and its relation to the surface geology, geologic evolution and the processes responsible for its formation.

4.4 Comparison to Landing Site Predictions

Evaluation of orbital information during landing site selection led to predictions of the surface characteristics, materials present and the geologic processes responsible for the formation and evolution of the site. During landing site selection for Mars Pathfinder (MPF), Mars Exploration Rover (MER), Phoenix (PHX), and Mars Science Laboratory (MSL), their remote sensing properties were compiled (Golombek et al. 1997b, 2003a, 2012a, 2017; Arvidson et al. 2008). After landing, characteristics of the surface were compared to those expected prior to landing (e.g., Golombek et al. 1999b, 2005). Specific comparisons included thermal inertia inferences of soil properties (cohesion) and particle sizes, the albedo and presence of bright dust, rock abundance, slopes, and radar inferences of bulk density and roughness. At MPF, PHX and Opportunity specific predictions of the geologic setting (MPF-catastrophic flood depositional plain, PHX-shallow ground ice, MER Opportunity-presence of hematite) were found to be correct with information collected after landing. Note that the geologic setting of surface observations will be aided by localizing the lander in orbital images, which is planned for InSight soon after landing (e.g., Folkner et al. 2018). Measurement of rocks from shadows in orbital HiRISE images (Golombek et al. 2008b, 2012b, 2017) and size-frequency distributions can also be compared with rock measurements from the surface (Golombek et al. 2003b, 2008b, 2012b). Specific predictions that have been made regarding surface characteristics, surface materials and their properties and the geologic processes responsible for their formation and evolution at the InSight landing site and tests that can be done after landing to confirm or reject these predictions are described in Sect. 6. The physical properties investigation (Sect. 5) also addresses some of these topics.

4.5 Thermophysical Properties

Thermal inertia values on Mars can be interpreted in terms of soil physical properties using analogous laboratory experiments and theoretical considerations. Thermal inertia (Piqueux and Christensen 2011) is defined as $I = (k\rho c)^{1/2}$, where k is the thermal conductivity, ρ is the bulk density of the surface material, and c is the specific heat. The thermal inertia represents the resistance to a change in temperature of the upper 2–30 cm of surface materials. While the density and specific heat capacity of geological materials vary only slightly (Neugebauer et al. 1971), thermal conductivity values range over several orders of magnitude and are controlled for the most part by the typical grain size (Presley and Christensen 1997a). As a result, grain sizes can be derived from thermal inertia values, and laboratory experiments have quantified this relationship (Presley and Christensen 1997b).

A surface layer composed of fine particles changes temperature quickly and so has a lower thermal inertia, whereas a surface layer composed of larger particles changes temperature more slowly and so has higher thermal inertia. Numerical modeling at the regolith grain scale have also been used to understand regolith density variations (Piqueux and Christensen 2011). In situ temperature measurements by rovers have been used to derive the thermal inertia and properties of surface materials (Fergason et al. 2006; Hamilton et al. 2014; Vasavada et al. 2017).

One other factor that may significantly impact the thermal inertia of the Martian regolith is cementation (Jakosky and Christensen 1986). Laboratory measurements (Presley and Christensen 1997a, 1997b, 1997c) and field measurements on Earth (Mellon et al. 2008) have demonstrated that small amounts of pore-filling cements can result in significant increases of thermal inertia values, and numerical theoretical work has quantified this effect (Piqueux and Christensen 2009). The mechanical properties seem similarly impacted, with mildly encrusted samples behaving mechanically like harder rocks (Piqueux and Christensen 2009).

The presence of rocks can also impact the interpretation of thermal inertia, even though rock abundance does not control the bulk thermal properties from orbit (Nowicki and Christensen 2007). Leveraging the large temperature contrast between rocks and fines during most of the Martian day and night, multi-wavelength observations can be used to deconvolve the contribution of various end-members and yield a rock abundance and fine component properties (Christensen 1986; Nowicki and Christensen 2007; Bandfield et al. 2011). Similarly, in the case of rovers and landers, the knowledge of the rock (or bedrock) areal fraction where temperatures are determined can be used to estimate the contribution of fines to the measured radiances, and help derive their thermal properties (Golombek et al. 2003b; Vasavada et al. 2017), resulting in a "rock-free" (or "fine-free" if the properties of rocks are assumed) derivation of the local thermophysical properties (similar to the fine component end-member derived from multi-wavelength analysis).

4.6 Eolian Features and Activity

Mars' surface marks the interface between geologic and atmospheric processes, which over time have resulted in a surficial layer with eolian features (e.g., Christensen and Moore 1992; Greeley et al. 2002). Depositional features include diverse sand dune morphologies (linear, barchan, star) and morphodynamics (transverse, longitudinal, oblique), ripples, wind shadows behind rocks, and wind streaks from craters (Greeley and Iversen 1985). Erosional features include yardangs, which form parallel to the prevailing wind, wind scoured rocks, and ventifacts. Much of our understanding of these features is based on terrestrial observations (Bagnold 1941; Greeley and Iversen 1985) and comparisons between Earth and other planets (Greeley and Iversen 1985). The formation times and spatial extent of these features cover a vast range of scales; from dust devil tracks formed in seconds to kilometer-scale dune fields formed over thousands of years. Some eolian bedforms on Mars are known to be active today, as movement has been observed in time-lapse orbital images (Bridges et al. 2013; Chojnacki et al. 2015), which can be used to infer information about the current wind regime and sediment fluxes. However, caution is required as there are also many examples of inactive or indurated bedforms, which do not necessarily relate to the modern wind field (e.g., Golombek et al. 2010).

For InSight we are primarily interested in small scale features that can be observed with the cameras near the lander and related to in-situ wind measurements. However, regional scale features that can be monitored from orbit are also important as they contain information about the global and regional time-averaged wind regimes, their diurnal and seasonal

variability, and how this relates to local wind conditions at the landing site (see Spiga et al. 2018, for an extended discussion on this topic).

Most eolian bedforms in the InSight landing ellipse are observed around fresh, rocky ejecta craters (Fig. 8). Most appear within the crater interior and trapped against the ejected rocks and crater rim. The majority appear bright, suggesting a coating of dust and recent inactivity. They lack clear sand dune morphology and appear similar to ripples observed by Spirit, Opportunity and Curiosity with a surficial layer of coarse granules and poorly sorted interiors. Bedforms and rocks are largely absent in the inter-crater regions, implying that rock and sand production, as well as recent sand mobilization and deposition, are limited to impact-proximal regions (Fig. 8). Dust devil tracks are common in HiRISE images with a dominant northwest trend (Fig. 8)

The formation of eolian features critically depends on the ability of the wind to lift small particles from the surface. This is essential for the formation of eolian erosional and depositional features, which requires a mobile sediment source and a significant increase in the abrasive power of the wind to form erosional features. The wind stress at the surface σ determines this transport and is given by:

$$\sigma = \rho u_*^2 \tag{1}$$

where ρ is the atmospheric density and u_* is the friction velocity. The friction velocity depends on the near surface wind profile and, assuming the simplest model for surface-atmosphere momentum exchanges, can be estimated from the scaling relation:

$$u(z) = \frac{u_*}{\kappa} \ln \frac{z}{z_0} \tag{2}$$

where $u(z)$ is wind velocity at distance z above the surface, $\kappa = 0.4$ is the Karman constant, and z_0 is the roughness length (Monin and Obukhov 1954). If the near surface wind profile can be measured for at least two heights then u_* and z_0 can be determined. Such a measurement was possible using the Pathfinder windsock experiment, which had three windsocks mounted on a mast at 33, 62, and 92 cm above the solar panels (Sullivan et al. 2000). This gave a value of $z_0 \sim 3$ cm for the Pathfinder landing site (Sullivan et al. 2000). The InSight landing site is considerably smoother (Sutton et al. 1978; Murdoch et al. 2017a, 2017b; Teanby et al. 2017). In the aerodynamic roughness length map inferred from orbital measurements by Hébrard et al. (2012), the InSight landing site is characterized by values of $z_0 \sim 0.1$–0.25 cm. IDC images will be used for assessing surface roughness, grain size distribution, and hence for estimating z_0 in the vicinity of the lander site.

To lift particles from the surface, the wind shear stress at the surface must exceed the saltation threshold. Once this threshold is exceeded, saltation can occur resulting in increased sediment transport for bedform creation. The lifting threshold can be estimated by comparing the measured movement of dune field ripples to predictions using GCM derived winds (Ayoub et al. 2014; Runyon et al. 2017). The best fit to observed ripple migration were obtained for a critical stress threshold of 0.01 ± 0.0015 N m^{-2}, which for a typical atmospheric density of 0.02 kg m^{-3} gives a corresponding u_* threshold u_{*t} of 0.7 m s^{-1}. This suggests saltation at the InSight landing site should be initiated for a windspeed of 10 m s^{-1} as measured at the height of the APSS wind sensor. Turbulence-resolving simulations for the InSight landing site described in Spiga et al. (2018) show that, even when the background wind is lower (5 m s^{-1}), friction velocity u_* larger than 0.7 m s^{-1} might be widespread in the afternoon, as a result of both convective vortices (possibly giving rise to dust devils) and convective gusts associated with convective cells.

The instantaneous particle transport flux τ is given by:

$$\begin{array}{ll} \tau \propto \rho u_*^2 (u_* - u_{*t}) & \text{if } u_* > u_{*t} \\ \tau = 0 & \text{otherwise} \end{array} \tag{3}$$

in the direction of the wind, so it strongly depends on wind speed. For a unidirectional wind regime and for large sediment availability, the most likely bedform is a transverse dune or ripple, with a bedform strike perpendicular to the wind vector (barchan dunes in the case of limited sediment supply). For varying wind speed and direction, the relationship is more complex (Courrech du Pont et al. 2014). In such cases, the average wind direction predicted by GCMs is often not well correlated to observed dune directions (Greeley et al. 1993; Hayward et al. 2007; Gardin et al. 2012). Recent laboratory experiments, numerical simulations and field measurements have demonstrated that a multidirectional wind regime can produce two dune trends depending on sand supply (Courrech du Pont et al. 2014; Gao et al. 2015; Lü et al. 2017). As shown by Courrech du Pont et al. (2014), this is because there are two competing dune growth mechanisms. (1) The bed instability mode: where there is no limit to sand supply (i.e., in transport-limited situations), dunes grow in height selecting the orientation for which the gross bedform-normal transport is maximum (Rubin and Hunter 1987). A modified version of this approach gave an improved match between GCM predicted winds and observed bedform orientations (Sefton-Nash et al. 2014). (2) The fingering mode: where the bed is partially starved of mobilizable sediment, dunes elongate in the direction of the resultant sand flux at their crest. Where dunes grow from fixed sources of sediment, this is the orientation for which the normal-to-crest components of transport cancel each other (Lucas et al. 2015; Gao et al. 2015). In transition areas from high to low sediment availability, the fingering mode is able to accurately predict the corresponding change in orientation of the dune crests under the same multidirectional wind regime (Fernandez-Cascales et al. 2018).

Many of the important parameters (e.g., u_*, u_{*t}, z_0, wind direction distribution) concerning the interaction of the atmosphere with surface transport and bedform formation are currently poorly constrained on Mars and strongly depend on local conditions. Comparing GCM and mesoscale wind predictions to orbital observations has allowed significant progress but would be much improved by combined surface wind measurements, saltation thresholds, and bedform observations from a long-lived surface station such as InSight.

The InSight lander offers the opportunity to study the activity of sediment transport (eolian and gravity-driven) in the vicinity of the lander not possible from previous landers. Knowing the initial conditions and analyzing imaging and wind time series, the eolian transport that occurs at the landing site can be investigated, through: (1) independent derivation of the sediment properties (e.g. Claudin and Andreotti 2006) (grain size distribution, cohesion, avalanche angle), (2) determination of the velocity threshold that initiates the eolian transport (Bridges et al. 2012), (3) measurements of the effect of bedform aspect ratio on the wind shear along the topography of the bedform (Courrech du Pont et al. 2014), and (4) measurements of the sediment flux at the landing site and any seasonal variations (Ayoub et al. 2014). All of these parameters are still unknown or largely debated but are fundamental for the understanding of sediment transport and bedform dynamics on Mars. Additionally, this science activity will be used in order to assess the saltation noise that will be recorded by SEIS.

In addition to potential bedforms that can be monitored by the cameras, the lander can be used for specific experiments related to sediment transport investigations. The IDA can be used to generate sand/soil piles of different size and aspect ratios next to the lander (Fig. 12). Those piles could be monitored with the cameras for generating time series of the piles and
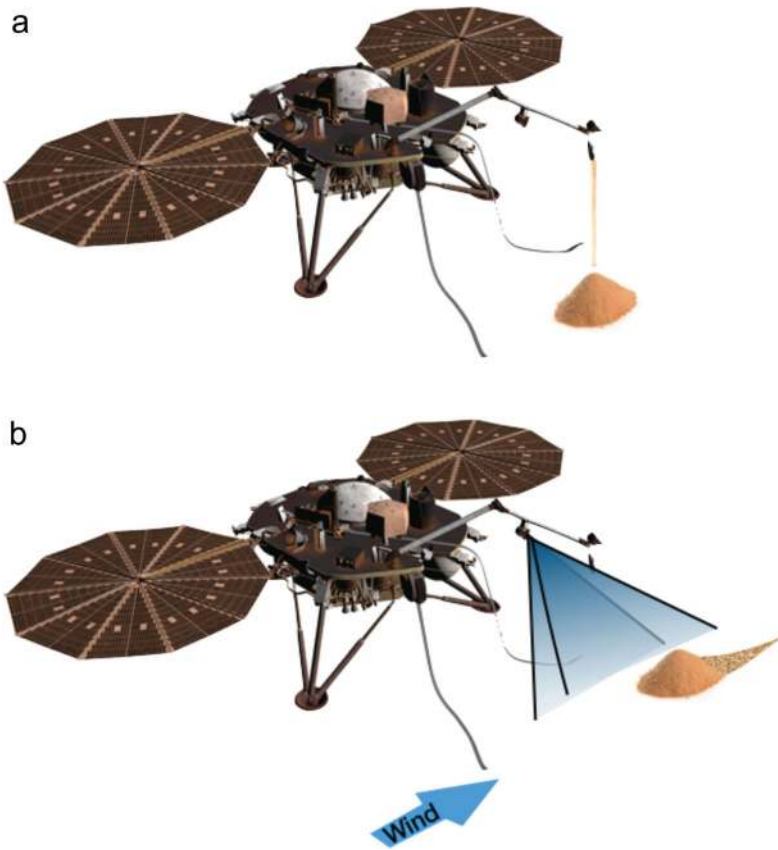
Fig. 12 (**a**) Sketch of a sand pile created with scoop and (**b**) after wind altered the pile

their immediate surroundings. Ideally the evolution of the shape of the piles may be tracked by taking stereo images at regular intervals or after the wind blows. Depending on the wind activity (as measured by APSS), if a sand pile were to migrate away from the lander, a second pile could be created. Wind data can be collected and combined with the camera images for time lapse monitoring of changes.

InSight will be uniquely suited to monitor the winds that might produce surface changes in that the wind sensors will be taking data continuously. If surface changes are detected, a complete record of the true peak winds that occurred during the interval containing the changes can be acquired, which will help establish an empirical threshold friction wind stress for grain motion. The area near the lander where imaging can detect subtle changes in surface topography can be used to identify changes to best constrain the threshold friction wind speeds (and through the estimated surface roughness, the threshold wind stress). Based on prior experiences with the previous landers, eolian change may be observed, particularly on soil that may be near the angle of repose. Stereo imaging sequences with the IDC will yield DEMs in the near vicinity of the lander (i.e., the workspace) with image resolutions on the order of ∼1 mm spatially and elevation postings of ∼5 mm.

From existing state-of-the-art atmospheric models (global climate and mesoscale models), the wind direction at the InSight landing site is predicted to be seasonally variable,

with multidirectional winds from the southeast, northwest and south. Transport modeling of near-surface winds indicates that active bedform crest lines should be oriented northeast-southwest (∼ 38–60° clockwise from north) from winds originating from the northwest, with possible large departures if the sediment supply is severely limited (details and references provided in Spiga et al. 2018). This is broadly consistent with the northeast orientation of eolian bedforms inside craters, the preponderance of bedforms to the northwest of fresh rocky ejecta crater rims, and the dominant northwest trend of dust devil tracks. Both the wind directions and bedform orientations can be verified, by measuring small ripples, small dunes, or modifications to regolith piles created by the scoop and rock wind shadow deposits.

4.7 Surface Alteration and Changes

4.7.1 Surface Modification During Landing

All previous landers on Mars have modified the surface during landing (e.g., Moore et al. 1987; Golombek et al. 1999a; Smith et al. 2009; Arvidson et al. 2004a, 2004b; Daubar et al. 2015). The InSight lander uses pulsed retropropulsive thrusters to slow itself during landing. These thrusters are the same as those used by the Phoenix lander, which dispersed 5–18 cm of soil when landing, exposing hard unaltered ice (Mehta et al. 2011). Modeling showed that pulsed thrusters lead to explosive erosion via cyclic shock waves that fluidize soils, producing ten times greater erosion than conventional jets (Mehta et al. 2011, 2013). For Phoenix, circular depressions of approximately 80 cm diameter and 13 cm depth formed where the exhaust plumes impinged on the surface. Conservative estimates of the maximum size of possible erosional depressions, generated by applying a conservation of momentum analysis, indicate upper limits of 1.6 m on the diameter and 40 cm on the depth of the depressions. The best estimate predictions of 1.1 m diameter and 18 cm depth are notably smaller than the bounding estimate. Although there should be negligible impact to the topography at the lander footpad locations or the instrument deployment zone (Golombek et al. 2017), surface soils will be dispersed away from the lander with sand and pebbles being eroded from the jet impingement locations and deposited away from the spacecraft. InSight will image the lander feet, the area beneath the lander and the surroundings, so the effects of surface modifications can be studied with regard to particles moved and depressions formed by the thrusters. Footpad penetration, erosional depressions, and dispersal pattern and particles will be related to the mechanical properties of the surface materials for InSight as has been done for previous landers (e.g., Moore et al. 1987; Golombek et al. 1999a; Arvidson et al. 2004a, 2004b; Mehta et al. 2011, 2013)

Of particular note, the landing site surface is likely covered with fine, high-albedo dust (Golombek et al. 2017) that will be displaced by the lander thrusters (e.g., Daubar et al. 2015; Mehta et al. 2013, 2011; Plemmons et al. 2008). As a result, the surface albedo will be lowered, as has occurred around previous landers. The albedo decrease can be expected to be intermediate between the cases of Phoenix and MSL based on measured changes in HiRISE images at these sites and their terrain properties (Daubar et al. 2015). For the MSL descent stage, the albedo was initially lowered by ∼50%. The majority of the darkened area faded to ∼90% of the surrounding albedo by ∼500 days after landing, but the darkest areas did not disappear completely in a few Mars years. The Phoenix landing reduced the albedo to ∼60–80% of the surrounding surface. Fading of the darkened area was incomplete due to seasonal imaging limitations at high latitude, but the darkened area disappeared completely over the first winter at the site (likely related to seasonal polar processes) (Daubar et al.

2015). Based on these observations, we expect the surface albedo at the InSight landing site will be reduced by ∼20–50% upon landing and then gradually return to the surrounding albedo over the next several Mars years.

4.7.2 Thermal Effects of Dust Removal

Dust removal during landing will increase the surface albedo (e.g. Daubar et al. 2015), thus changing the surface energy balance (Plesa et al. 2016). The resulting surface cooling will cause an instantaneous drop of the average daily surface temperature, and this signal will slowly diffuse into the subsurface, temporarily increasing the subsurface thermal gradient (Grott et al. 2007; Grott 2009). This will need to be taken into account when inverting HP^3 data taken at depths down to 3 m below the surface, but deeper temperature readings should remain unaffected. In addition, the speed with which the perturbation travels into the subsurface holds clues to the regolith thermal diffusivity, which is defined as $\kappa = k/\rho c$, where k is thermal conductivity, ρ is density, and c is specific heat. As thermal conductivity is directly measured by the HP^3 instrument and c can be considered to be reasonably well constrained, the temperature response to the sudden cooling caused by dust removal can likely be interpreted in terms of the average regolith density.

4.7.3 Dust Deposition on Solar Panels

Dust has been observed to be deposited on the solar panels of all solar powered landers and rovers on Mars. On Mars Pathfinder, The Mars Adherence Experiment was designed to measure the rate of settling of dust onto the solar arrays and found an obscuration and reduction in solar power generated by the arrays of 0.28% per day (Landis and Jenkins 2000). Both MERs also experienced dust deposited on their solar panels that correlated with changes in dust opacity in the atmosphere (Stella and Herman 2010; Vaughan et al. 2010). Because MER also measured the atmospheric opacity (Lemmon et al. 2004), the amount of dust on the solar panels (the dust factor) was also derived (Stella and Herman 2010). These data recorded differences in dust cleaning events between the rovers that are likely due to wind vortices or dust devils (Lorenz and Reiss 2015). Phoenix similarly recorded dust deposition onto the spacecraft from the atmosphere (Drube et al. 2010). InSight will measure atmospheric opacity with the IDC (Maki et al. 2018) and so will be able to determine the amount of dust on the solar panels similar to MER.

4.7.4 Dust Devils

Reiss and Lorenz (2016) reported a survey of dust devil tracks in the Elysium Planitia landing region for InSight and noted that the observed tracks tended to be considerably smaller (< 10 m width) than those measured by Verba et al. (2010) at the Gusev site (mean width ∼56 m) for Spirit. Crudely equating dust devil activity with evidence of tracks (an imperfect association, since visible track formation depends on the presence of a thin dust layer that can be removed by a vortex, as well as on the vortices themselves) suggests that InSight will observe dust devil activity intermediate between Spirit (which observed many dust devils) and Curiosity, which has observed relatively few (e.g., Moores et al. 2015). The track formation rate of between 0.002 and 0.08 tracks per square kilometer per sol, coupled with the observed lengths and widths, suggests that track-forming (and by analogy, solar-panel-clearing, Lorenz and Reiss 2015) vortex encounters with a lander may have a recurrence interval of some years (much longer than the couple of hundred days encountered by Spirit).

If true, solar power degradation by dust accumulation on InSight's solar arrays may not be mitigated by dust devil cleaning events as often as was the case for Spirit. However, the similarity in dust cover index (Ruff and Christensen 2002) and albedo of the InSight and Spirit landing sites (Golombek et al. 2017) suggests similar amounts of dust on the surface and a similar rate of removal of dust given that the rate of dust settling out of the atmosphere is fairly constant for a given opacity (Stella and Herman 2010).

In general, dust devil tracks are rather straight, suggesting motion dominated by a prevailing wind or meandering or even looping (cycloidal). It seems probable that this property (sinuosity—the ratio of the along-track length to the straight-line start-to-end distance) may be indicative of typical wind conditions. The tracks studied by Reiss and Lorenz (2016) were predominantly straight and have a rather narrow azimuth distribution (northwest/southeast) suggesting that winds are relatively strong and uniform in direction when dust devils form. This consistent migration direction may permit strategies for dust devil detection by imaging to be optimized for maximizing counts of overall activity (looking upwind) if images are limited due to data volume constraints. On the other hand, if many images can be taken, looking orthogonal to the wind would maximize information on size, distance and migration rate for individual encounters. These parameters would also be useful in interpreting geophysical signatures of dust devils (e.g., the stiffness of the ground from the elastic deformation induced by the negative load of the passing vortex, e.g. Lorenz et al. 2015 and Sect. 5.4).

4.7.5 Images for Change Detection

Repeated orbital images will benefit several different InSight investigations. The 25-cm/pixel scale and excellent signal to noise ratio of HiRISE (McEwen et al. 2007) on MRO, is capable of detecting changes at scales comparable to those able to be investigated by the lander. Specifically, eolian bedform migration near the lander detected from orbit can be ground-truthed with images from InSight cameras. The relative albedo of the landing site will be monitored from orbit for fading of the landing-induced darkening using HiRISE (e.g., Daubar et al. 2015), but also perhaps by Compact Reconnaissance Imaging Spectrometer for Mars (CRISM) at 18 m/pixel (e.g., Seelos et al. 2014) and Colour and Stereo Imaging System (CaSSIS) at 5 m/pixel (Thomas et al. 2017). Brightening will also be monitored by the lander's cameras (Maki et al. 2018) allowing comparison between orbital and ground-based images. Dust devils passing close to the lander are expected to be detected with the lander instrumentation as well, so orbital images will also be searched for the appearance of new dust devil tracks (or perhaps even a dust devil itself in the meteorology data).

4.8 Selecting Instrument Placement Sites

After landing and assessment of the condition of the lander, the most important activity is placing the instruments onto the surface as quickly as possible (Banerdt et al. 2018). Project surface operations scenarios allocate approximately 50 sols for deploying the SEIS, WTS and HP³ within a crescent-shaped workspace that can be reached by the arm. During the first two weeks, the Instrument Site Selection Working Group (ISSWG) must decide where to place the instruments in the workspace based on the spacecraft tilt, workspace topography, surface characteristics (soils, rocks, etc.) and instrument placement requirements (Banerdt et al. 2018; Abarca et al. 2018). Because the instruments must be placed on relatively flat, rock free locations that are load bearing, assessment of surface characteristics relies extensively on the geology and physical properties of surface materials in the workspace.

Two subgroups of ISSWG will carry out these investigations (Banerdt et al. 2018). The geology subgroup will evaluate the surficial geology and map soils, rocks, eolian bedforms and other geological features such as craters. The physical properties subgroup will derive the thermal inertia from hourly radiometer measurements of two spots on the surface (which are on the opposite side, north of the lander from the instrument deployment workspace), separate the rocky from fine component of the thermal inertia from stereo surface images and measurements of their areal contributions, and estimate particle size and/or cohesion of the fine component to determine if the soil is load bearing. The soil maps from the geology subgroup allow the extrapolation of physical properties to similar materials in the workspace.

5 Physical Properties Investigation

5.1 Physical Properties of Surface Materials

The physical properties of soils, such as thermal conductivity, dielectric constant, seismic velocities, compressibility, shear strength, and penetration resistance depend on its bulk density, which depends on the grain size distribution, grain roundness, angularity, void ratio, porosity, and particle arrangement (Carrier et al. 1973). Bulk density affects all mechanical properties, including the elastic parameters (Young's modulus, E, the shear modulus, G, and Poisson's ratio, ν). As an example, the Young's modulus of loose Hostun sand (France) determined from triaxial tests at 0.1% axial deformation range (void ratio, $D_r = 0.14$, bulk density $\rho = 1392$ kg/m^3) is between 10 MPa under a confining stress of 20 kPa, and 30 MPa under 100 kPa. If dense ($D_r = 0.88$, $\rho = 1721$ kg/m^3), it ranges between 16 MPa (under 20 kPa) and 46 MPa (under 100 kPa) (Lancelot et al. 1996), which demonstrates the stress dependency of Young modulus in granular materials. Note also that the elastic modulus of sand is strain dependent, with higher values at low strains (Atkinson and Sallfors 1991). In this regard, the elastic shear modulus governing the propagation of elastic waves (strains smaller than 10^{-3}%) in sand is significantly higher than that governing the interaction of instruments (SEIS, mole, or scoop) with the ground (strains larger than 5×10^{-2}%).

Once elastic deformation is exceeded by the stress field applied (around the mole during penetration or during scoop operations, for example), irreversible plastic deformation occurs, with changes in the arrangement of grains. Depending on the bulk density, sand submitted to shear may either contract (loose sand) or expand (dense sand), prior to failure. As a consequence, penetration is much easier in loose sand than in dense sand. Finally, when failure occurs in cohesionless sand, its geometry is controlled by the angle of internal friction, which also depends on the bulk density.

The most common failure criterion used for granular materials is the Mohr-Coulomb criterion (Holtz and Kovacs 1981). This criterion is defined by the angle of internal friction, ϕ, and cohesion, c, when the grains are bonded together. The friction angle defines a linear relationship between shear failure and the confining pressure of a granular material. As an example, Lee and Seed (1967) measured a friction angle for rounded Sacramento river sand that ranges between 34° (at a density of 1440 kg/m^3) and 41° (at 1680 kg/m^3). The friction angle can be related to the angle of repose for cohesionless materials. In granular materials in which some bonding has developed between the grains, the cohesion is a constant that is independent of the confining pressure. These failure parameters are dependent on the state of the regolith including relative density, particle size distribution, roundness, angularity, cementation and many other properties. Subsequent sections detail experiments for the InSight mission to capture elastic and failure

properties of martian surface materials. Basic soil parameters of martian surface materials have been derived from all previous landed missions (e.g., Christensen and Moore 1992; Herkenhoff et al. 2008), either by interaction of arms on Viking (Moore et al. 1987) and Phoenix (Shaw et al. 2009) missions, or by interaction of wheels with the surface soils by the MPF (Moore et al. 1999), MER (Arvidson et al. 2004a, 2004b; Sullivan et al. 2011) or MSL (Arvidson et al. 2014) rovers.

5.2 Simulants

Earth simulants have been used to conduct laboratory tests to constrain the likely physical properties of soils on Mars in preparation for the InSight mission (Delage et al. 2017). These tests include one dimensional compression, shear, and measurement of seismic P- and S-wave velocities and have been compared to other terrestrial sands and their physical properties. Two materials used in the tests bound the likely size distribution of soils on Mars and include: a mix of Mojave Mars Simulant (MMS, Peters et al. 2008), which is crushed Miocene basalt, with local alluvial sedimentary and igneous grains, and Eifelsand simulant, which is a mix of crushed basalt and volcanic pumice sand. The behavior of a finer Mars Soil Simulant-Dust (MSS-D, Becker and Vrettos 2016), which is an equal mix of crushed olivine and quartz sand with a bimodal grain size distribution curve with one mode smaller than sand (powder), was also investigated.

Unlike lunar regolith, which is composed of angular particles due to impact comminution from basin size to single atoms, sand on Mars is generally rounded because the smallest impacts are filtered out by the atmosphere (e.g., Paige et al. 2007) and sand grains are mobilized by the wind and saltation rounds the grains (e.g., McGlynn et al. 2011; Goetz et al. 2010; Minitti et al. 2013; Ehlmann et al. 2018). As a result, shear tests carried out on lunar regolith (Scott 1987) or lunar regolith simulants (JSC-1 simulant or other crushed basalts, e.g., McKay et al. 1994; Alshibli and Hasan 2009; Vrettos 2012; Vrettos et al. 2014) may not be entirely relevant, given that the highly angular shape of the grains results in larger friction angles. Note also that some Mars regolith simulants, like JSC Mars 1 (Seiferlin et al. 2008), which is based on mineralogical similarity and made up of weathered volcanic ash also has irregular grain shapes, and thus could have a different mechanical response from sand with rounded grains. In this regard, simulants based on quartz sand on Earth (e.g., WF34, Lichtenheldt et al. 2014), which is typically rounded by fluvial, marine and eolian activity, may be mechanically more representative of soils on Mars that are dominated by rounded and equant basaltic sand grains.

5.3 Physical Properties from HP^3 and Mole Modeling

The penetration progress achieved by the HP^3 mole per stroke depends on the mechanical properties of the regolith (Sect. 2.3), and mole progress can be interpreted similar to dynamic penetration or a pile-driving processes. To translate the penetration speed to mechanical soil parameters like the angle of internal friction and density, different types of models can be used. In the simplest form, analytical models couple energy input into the soil with a soil mechanics model, but more realistic models consider the detailed action of the mole hammering mechanism (Lichtenheldt et al. 2014) together with the soil's mechanical response. The latter may be treated by either soil physics models (Lichtenheldt and Krömer 2016; Kömle et al. 2015; Poganski et al. 2017b) or Discrete Element Models (DE Models, Lichtenheldt et al. 2014; Lichtenheldt 2015, 2017; Poganski et al. 2017a), which are, however,
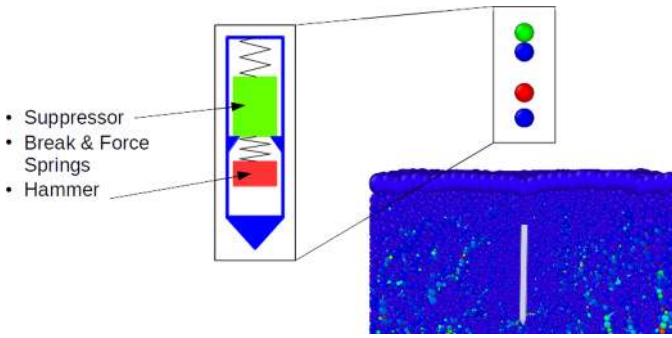
Fig. 13 Implementation of HP[3] mole hammering within the DE Model. On the left side of the panel a schematic representation of the mole hammer mechanism shows the hammer mass (red), the support mass above it (green) and the mole housing (blue). The hammer and support mass are connected by springs that can transfer energy to the mole housing. On the upper right side is the corresponding implementation of the hammer mechanism within the DE Model. The hammer model is rigidly connected with the mole body in the soil model (lower right panel). Thus a more realistic hammer force can be computed from the interaction of the hammer mechanism, mole body and the surrounding soil. The colors in the lower right panel show the residual stress when the mole is not moving, with red indicating a higher stress and blue no stress

computationally demanding. As a result, DE Models are used for the detailed study of single or few hammering strokes. The DE Model is a particle-based method that can simulate the dynamics of the interaction of the mole with the surrounding regolith and thus provides mole penetration progress and force profiles with depths. These force profiles can be used as input to pile driving (Poganski et al. 2017a) and soil physics (Lichtenheldt and Krömer 2016) models, which can simulate the entire penetration of the mole. The DE Models are either calibrated by tuning properties to standard laboratory tests using a quartz sand simulant (Poganski et al. 2017a), or by using a direct, systematic identification strategy (Lichtenheldt 2015) with quartz sand (WF34, see Lichtenheldt 2016).

To initialize a DE Model, a volume is filled with particles at an assumed packing density. The depth of the simulation volume is either determined by a layer of coarse particles with a weight corresponding to the overburden pressure for this depth at the local gravity (Poganski et al. 2017b) or by retaining the overburden pressure by loading and deleting particles (dynamic boundaries, Lichtenheldt 2017) as the mole is driven into the soil. The overburden pressure is then retained by fixing the boundary particles. The body of the HP[3] mole is then either placed at the top of the volume (surface penetration) or is embedded within the volume for deeper layers (Fig. 13). The hammering mechanism is implemented either using four masses simplifying the hammering mechanism (Poganski et al. 2017a) or using a complex, enhanced multi-body model of the mole hammering mechanism (Lichtenheldt et al. 2014; Lichtenheldt 2017).

A typical hammering cycle consists of multiple hits by either the hammer or the support mass on the mole casing where the second hit in the cycle is generated by the rebound of the support mass (see Lichtenheldt et al. 2014; Lichtenheldt 2016). For any given depth, the force profile of a hammering cycle can be reproduced with these DE Models. Using the model by Lichtenheldt (2017) it was also possible to simulate the wave propagation in the regolith caused by the hammering strokes (Fig. 14).

The soil physics models will be used in an approach similar to that of Poganski et al. (2017b) to calculate the model parameters from the physical soil parameters while at the same time taking the mole geometry into account. Given the soil model parameters, coupling of the mole model with the soil model will provide the per-stroke performance of the mole
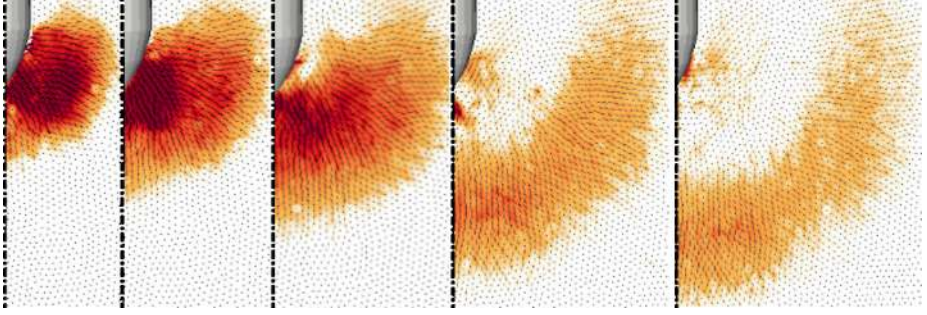
Fig. 14 Wave propagation through the soil 2, 3, 4, 6 and 7 ms after the first stroke of the HP^3 mole's hammering cycle on Mars (Lichtenheldt 2017). The result has been generated by using the model coupling enhanced multi-body dynamics of the hammering mechanism and the DE Model presented in Lichtenheldt et al. (2014) and Lichtenheldt (2017) (further details in Lichtenheldt 2016). The wave fronts are colored by the interpolated particle velocities. The mole is shown in grey in the upper left; red and darker colors corresponds to faster particles, whereas lighter red/orange and yellow colors are for slower particles. Particle velocities in white are below the threshold
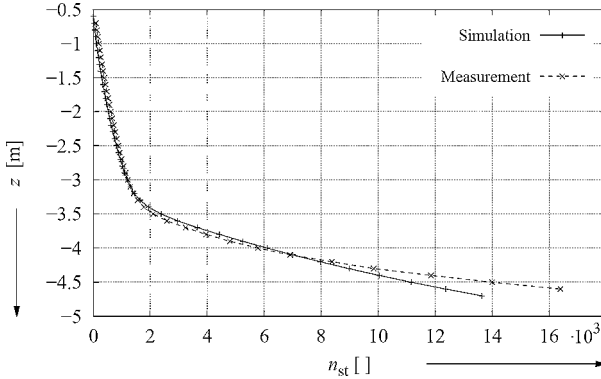
Fig. 15 Comparison between number of hammering strokes, n_{st}, and the depth measured during a deep penetration test of the HP^3 mole in WF-34 quartz sand (DPT#3, Spohn et al. 2018) and simulated using the soil physics model of Lichtenheldt and Krömer (2016). The quartz sand had a measured density, ρ of 1460 ± 100 kg m^{-3} and a friction angle, ϕ of 30.3 ± 0.3 °. The simulation uses $\phi = 30.9$ ° and $\rho = 1492$ kg m^{-3} as average values for the depth profile, which were identified using the depth dependent strategy described in the text. The regolith parameters of the simulation are varied with depth in the range of $\phi = 22$–42 ° and $\rho = 1350$–1650 kg m^{-3}. The decrease in rate of penetration of the mole at 3.4 m is produced by an increase in friction angle and bulk density up to their maximum values between 3 m and 3.4 m depth

at prescribed depths, from which the overall penetration progress can be reconstructed (e.g., Fig. 15). In this manner, soil properties in the simulation can be matched to the measured penetration of the mole, yielding tight constraints on both the soil density and angle of internal friction.

Due to the complex nature of operating a hammering mechanism inside a non-linear, anisotropic, non-continuous and possibly inhomogeneous soil, a direct inversion of the models for soil parameters is not feasible. Thus, parameter estimation poses an optimization problem to minimize the error between the measured and simulated progress using angle of internal friction, ϕ and density, ρ as free parameters. Both parameters can be assumed

to be bounded over a reasonable range, but trade-offs between ϕ and ρ exist. In addition, knowledge gathered from laboratory experiments on the relationship of $\phi(\rho)$ (Delage et al. 2017) will help to narrow down the range of admissible parameters (e.g., progress is much less sensitive to changes of ρ as compared to changes of ϕ). For constant density, inversion of the mole penetration curve could be carried out by fitting the entire depth range simultaneously, but it is expected that parameters will vary with depth. Therefore, we plan to use a stepwise inversion of the penetration curve considering small depth intervals individually. Each depth interval will be considered as a separate optimization problem, and continuity conditions will be imposed to adjacent sections. In summary, we will thus obtain estimates of density $\rho(z)$ along with estimates of the internal friction angle $\phi(\rho)$ as a function of density. For the pile driving model, a parameter tuning approach is carried out to match the mole penetration on Mars.

5.4 Physical Properties from Passive SEIS Monitoring

5.4.1 Physical Properties and Regolith Structure

Physical properties of the regolith at the landing site, specifically the seismic velocity profile, can also be constrained by data collected during passive SEIS monitoring. Constrains on deeper structure from the analysis of seismic signals associated with marsquakes and impacts are developed in Panning et al. (2017); this section mostly discusses signals caused by local atmospheric disturbances that might be a significant source of high frequency seismic noise and ground deformation.

As observed in terrestrial field data (Lorenz et al. 2015) and derived from analysis of large eddy simulations for realistic landing site conditions (Kenda et al. 2017), pressure fluctuations associated with dust devils or non-dust carrying convective vortices passing within a few hundred m of a sensitive broad-band seismometer induce measurable tilt at long periods (i.e., < 10 s, Mimoun et al. 2017; Murdoch et al. 2017a). The spectral ratio between this ground tilt and the pressure time series, available from APSS for InSight, depends on the elastic parameters of the subsurface (Sorrells et al. 1971), with a larger tilt generated for material with lower rigidity. The frequency-dependent ratio can thus be used to distinguish between different models of subsurface structure (e.g., regolith thickness) (Kenda et al. 2017).

Seismic velocities and regolith thickness at the landing site can also be derived from observations of high-frequency surface waves above 1 Hz, based on two complimentary approaches. High-frequency seismic signals related to passing dust devils have been observed on Earth (Lorenz et al. 2015) and identified as shallow surface waves. Kenda et al. (2017) have demonstrated that modeling high-energy spectral lines in these signals as multi-mode Rayleigh wave Airy phases (i.e., extrema in group velocity dispersion curves) can constrain subsurface S-wave velocities. In addition, if the trajectory of the dust devil is constrained, for example by orbital observation of the track, the arrival time difference between surface waves and atmospheric infrasound (Lorenz et al. 2015; Lorenz and Christie 2015) would constrain the surface-wave velocity, as the sound speed in the martian atmosphere is known (Kenda et al. 2017).

Furthermore, parts of the ambient wavefield that are dominated by Rayleigh waves can be extracted from SEIS recordings and used to measure the elliptical Rayleigh wave polarization by computing the horizontal-to-vertical spectral ratio (Hobiger et al. 2012). As shown by Knapmeyer-Endrun et al. (2017, 2018), Rayleigh wave ellipticity of both the fundamental and, to a lesser degree, the first higher mode can be measured for a reasonable subsurface

model of the landing site and provide additional information on P- and S-wave velocities and shallow subsurface layering. If some initial constraints (e.g., from laboratory velocity measurements), orbital regolith thickness mapping (see Sect. 3.4), or analysis of HP³ seismic signals (Kedar et al. 2017) are available, Rayleigh wave ellipticity inversion can supply information on the thickness and velocities of the sub-regolith layer (Knapmeyer-Endrun et al. 2017). Furthermore, the data can potentially distinguish between a constant velocity in the regolith and a velocity that increases with depth (Knapmeyer-Endrun et al. 2017).

The mechanical noise of the lander, transmitted through the ground to the seismometer (Murdoch et al. 2017b), may provide an additional method for determination of the ground physical properties through passive monitoring. As the frequencies of the lander resonances will be related to the ground stiffness under the lander feet, the most promising method for this is likely to be through identification of the frequencies of these resonances. Although many of the lander resonance frequencies are far above the VBB bandwidth (by design), and many are even above the SP bandwidth, some resonant frequencies may still be observable within the limits of the instrument sampling frequency.

On a global scale, the cut-off frequency of spectra of impact recordings, i.e. the frequency where a sloping asymptote of the acceleration spectral density at low frequencies changes to a flat plateau at high frequencies, can be used to approximate regolith thickness and porosity at an impact site, as it is inversely proportional to the impact shock wave radiation in the regolith. The method has been demonstrated for Apollo lunar data by Gudkova et al. (2011, 2015), and application to SEIS would allow gathering information on regolith properties and their variability away from the landing site (e.g., Daubar et al. 2018).

5.4.2 Elastic properties from LVL Stiffness

Both sensors of the SEIS instrument (VBBs and SPs) are mounted on the mechanical leveling system (LVL), whose feet are in contact with the martian surface. The length of the three LVL legs can be adjusted independently to level the SEIS sensors at ground tilts of up to ∼15 °. During qualification tests, horizontal resonances of the LVL were observed at frequencies between 35 and 50 Hz, depending on the LVL configuration (Fayon et al. 2018). The resonance frequencies depend on the length of each of the LVL legs, but also on the mechanical coupling between the feet and the ground. The LVL resonance frequencies observed on Mars may thus provide additional information on the physical properties of the top-most ∼2–3 cm of soil at the InSight landing site.

To interpret the LVL's structural resonances, a simplified analytical structural model of the LVL has been developed (Fayon et al. 2018). This model can reproduce the LVL's mechanical behavior (i.e., its resonance frequencies and transfer function), and can be used to infer the strength of the coupling with the ground by fitting the observed resonances. The modeling approach is based on a study that detects and compensates for inconsistent coupling conditions during seismic acquisition with geophones (Bagaini and Barajas-Olalde 2007). Four main structural elements characterize the LVL model: one platform and three legs. The mechanical links between the different elements are modeled as springs with strengths derived from mechanical tests. The parameter of interest, the foot-ground coupling, is described by two variables k_v^g and k_h^g, which indicate the stiffness of the vertical and horizontal elastic forces between the feet and the ground. Tests have shown that this model can correctly describe the eigenmodes and the transfer function of the structure. Its sensitivity to different model parameters has been studied by changing various parameters such as the mass of the platform, the length of each leg, the stiffness of the springs, the torque between the ground and the legs, and the attenuation coefficient, Q, of the elastic forces between the legs and the ground.

Simulations with different configurations consistently show that only two of the 21 possible vibrational modes of the LVL (resonances and displacements of the structure) have frequencies within the range covered by the SEIS sensors (Fayon et al. 2018). These two modes correspond to horizontal translations of the platform in X- and Y-direction, respectively, in agreement with the LVL resonances observed in qualification tests. The simulations also show that SEIS, including the LVL and its legs, can be assumed to be perfectly rigid within the frequency band covered by the seismometers, and that the internal mechanical links (i.e., the stiffness of the springs between the platform and the legs in the model) do not affect the resonance frequencies. In contrast, the parameters k_h^g and C_h^g, related to the horizontal elastic force and torque between the feet and the ground, respectively, control the horizontal resonances at frequencies below 50 Hz (i.e., within the range covered by SEIS at its highest acquisition rate of 100 Hz). The link between these two parameters and the regolith's physical properties (Poisson ratio, ν, and Young's modulus, E) can be analytically expressed for the case of a simple circular plate with radius a on a semi-infinite mass (Poulos and Davis 1974):

$$k_h^g = \frac{16(1-\nu)Ea}{(7-8\nu)(1+\nu)} \tag{4}$$

$$C_h^g = \frac{4Ea^3}{3(1-\nu^2)} \tag{5}$$

However, the presence of cones on the LVL feet complicates the direct application of these equations. More complete expressions for feet with cones will be derived from additional experiments to invert the LVL's resonance frequencies measured on Mars in terms of physical properties of the regolith (Fayon et al. 2018).

5.5 Physical Properties from HP³-SEIS Hammering

The InSight team has developed a variety of algorithms summarized in Kedar et al. (2017) to use the multitude of HP³ hammer strokes to extract the elastic physical properties of the shallow subsurface: P-, and S-wave velocities, Q, as well as the thickness of the regolith layer and possibly even of the shallowest bedrock units. An adapted seismic-data acquisition combining the SP signals in the 50–100 Hz frequency band with the VBB recordings at frequencies below 50 Hz will allow increasing the temporal resolution of the SEIS data measured during the HP³ experiment (Lognonné et al. 2018). The processing of the HP³ seismic signals will involve the analysis of the travel-times and amplitudes of the recorded seismic arrivals. As discussed in Kedar et al. (2017), the travel-times of the observed first P- and S-wave phases should enable the determination of the local P- and S-wave velocities at the mole location. The analysis of direct and reflected wave amplitudes and full-waveform inversion may allow increasing the resolution of the seismic velocity structure to depths below the maximum penetration depth of the mole as well as the extraction of seismic attenuation.

The geometry of the HP³ experiment with the seismic source (mole) at depth and the receiver located at the surface closely resembles a reverse vertical-seismic profiling (reverse VSP) experiment. Established active seismic-exploration processing techniques can be used to isolate reflections and transform the reflection information into subsurface images (Hardage 2000). Figure 16 displays the resultant P-wave seismic-reflection image from processing simulated SEIS recordings for the HP³ experiment. A layered near-surface velocity, density and attenuation (Q) model including interfaces at 5 m marking the transition from relatively fine-grained regolith to coarse ejecta, at 11 m to fractured basalt, and at 24 m
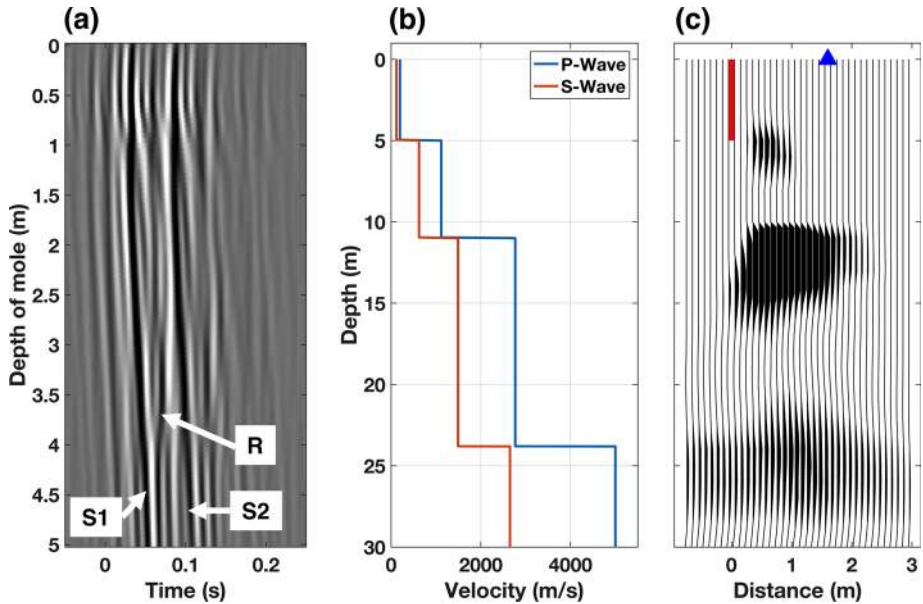
Fig. 16 (**a**) Simulated waveform data for the HP³ experiment recorded with the sampling strategy outlined in Lognonné et al. (2018). S1 and S2 mark the two hits of one hammering cycle (see Lichtenheldt et al. 2014) and R denotes a reflection. (**b**) P- and S-wave velocity structure used for the simulation. (**c**) Final processed seismic-reflection image. The red line marks the trajectory of the HP³ mole penetrating from the surface to 5 m depth, the blue triangle marks the location of the SEIS instrument and the black wiggles correspond to the three subsurface interfaces

to intact basalt (Knapmeyer-Endrun et al. 2018), served as input to the finite-element modeling (Fig. 16b). Conventional VSP processing steps such as separating the direct waves from reflected waves and Kirchhoff depth migration were employed.

In this idealized setting (e.g., noise free data and correct P-wave velocity used for migration), all three interfaces of the input model including the deepest interface at 24 m depth can be resolved (Fig. 16c). Multi-component seismic imaging techniques may allow producing images of S-wave reflections and P-to-S- and S-to-P-wave conversions (Reiser et al. 2018).

5.6 Physical Properties from Arm Experiments

The IDA is equipped with a bucket-like scoop mounted on the end. This scoop can be used in evaluating regolith mechanical properties at the InSight landing site. Specifically, forces acting on the IDA can be monitored via the motor currents in the arm in a similar fashion to mechanical measurements with the Viking and Phoenix lander robotic arms (Moore et al. 1987; Shaw et al. 2009). Additionally, regolith can be manipulated into piles to determine some of its inherent properties. An overview of the proposed experiments is shown in Fig. 17.

These experiments can be calibrated in a JPL testbed for InSight activities (Trebi-Ollennu et al. 2018) and with numerical simulations described below.

5.6.1 Scraping and Trenching

The IDA has a scoop that can be used to conduct backhoe-style trenching, scraping, and scooping activities at the landing site (Fig. 17). Similar tests were conducted during the

Fig. 17 Overview of soil mechanics tests that could be conducted with IDA showing (**A**) scraping, (**B**) piling, (**C**) indentation, and (**D**) HP^3-SEIS hammering
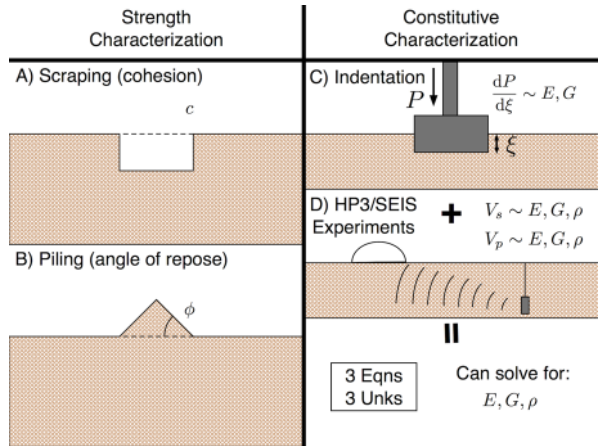
Viking and Phoenix missions (Moore et al. 1987; Shaw et al. 2009), which used methods that had been used for lunar soils (Wilkinson and DeGennaro 2007). In that work, force data during scooping operations was measured directly from motor currents. These data combined with relative positioning data during scooping (measured to within 2 mm) for location and scooping depth can directly be used to calculate the cohesion similar to Phoenix (Shaw et al. 2009).

5.6.2 Piling

The material scooped up by the arm during trenching or scraping can also be used to create a pile, which can be observed by the cameras. Multiple scoops and dumping procedures could build up larger piles. The angle of the pile of cohesionless material is the angle of repose, ϕ_a (related to the friction angle), and can be measured from DEMs produced from stereo images (Carrigy 1970; Horstman and Melosh 1989). An example of a pile and the measured angle is shown in Fig. 17B. The angle of repose is important for characterizing a regolith and directly relates to other scientific investigations on Mars including the slope of the slip face of sand dunes.

5.6.3 Indentation

In perhaps the conceptually simplest experiment, but most challenging to implement, the flat part of the scoop can be pushed into the ground (Fig. 17C). Utilizing the IDA's relative positioning and currents, the depth of penetration (ξ) and indentation force (P) can be measured. These quantities are directly related to the elastic properties, Young's modulus (E) and the shear modulus (G), through Boussinesq's formula. We utilize the equations derived by Pharr et al. (1992) and shown in Eq. (6).

$$\frac{dP}{d\xi} = \beta \frac{2}{\sqrt{\pi}} \sqrt{A} E_r \tag{6}$$

Specifically, the derivative of the load with respect to the displacement is calculated during the initial elastic unloading phase upon lifting the scoop after indentation. β is the scoop's geometric indentation shape factor (e.g. circle = 1, triangle = 1.034, square = 1.012), which

will be calculated for the arbitrary, but specific geometry that works best in the testbed for the IDA. A is the area of the indentation shape. E_r is the reduced modulus of elasticity, which relates regolith material properties (E, ν) to the scoop's material properties (E_s, ν_s) in Eq. (7).

$$\frac{1}{E_r} = \frac{1 - \nu^2}{E} + \frac{1 - \nu_s^2}{E_s} \tag{7}$$

The optimal solution for the scoop's punching shape can be selected through testing. When combined with Eqs. (8) and (9), which are directly calculated from the SEIS and HP^3 experiments detailed in previous sections, a system of three equations and three unknowns can be set up to solve for the elastic properties (any 2 of E, G, ν, and λ, Lamé constant) and density, ρ of the Martian regolith at the landing site. These properties are classic quantities used on Earth for engineering design/analysis and would be particularly useful for future planned missions to Mars.

$$V_P = \sqrt{\frac{\lambda + 2G}{\rho}} \tag{8}$$

$$V_S = \sqrt{\frac{G}{\rho}} \tag{9}$$

5.6.4 SEIS Tilt During Indentation

During indentation experiments the resulting tilt can be measured by SEIS. Using an elastic ground deformation model (e.g., Murdoch et al. 2017a, 2017b), we calculate that for a 50 N vertical force applied on the ground by the robotic arm scoop, the apparent horizontal acceleration on SEIS due to the tilt is estimated to be 2.3×10^{-7}, 5.0×10^{-7} and 1.7×10^{-6} m s^{-2} at distances of 1.5 m, 1 m and 0.5 m from the closest SEIS foot, respectively. These acceleration amplitudes should be easily detectable by SEIS given the noise level requirement of 2.5×10^{-9} m s^{-2} (Mimoun et al. 2017).

The elastic ground parameters (shear modulus, Poisson's ratio, Young's modulus) can be constrained by solving a system of nonlinear equations derived from the elastic ground deformation model. The inputs would be the measured and known parameters (i.e., the relative position of the three SEIS feet and the lander scoop on the ground, the vertical force applied by the lander scoop, and the resulting tilt of SEIS). In addition to the elastic measurements, if the ground can be imaged with the IDC before and after the experiment, the observed plastic deformation of the regolith will provide further information on the material strength and porosity.

5.6.5 Numerical Models of Arm Interactions

The same DE Model code discussed in Sect. 5.3 was used to model the mechanical interaction of the IDA scoop with the regolith (Fig. 18). Computational time was reduced by using grains larger than the actual size, while maintaining a similar size ratio to the actual particle size distribution. The scoop was implemented as a geometrically realistic, but simplified mesh model with the motion of the mesh controlled by a script during the model run. Thus, simple actions like indentations or more complex trenching and piling can be modeled. These model runs can deliver two basic types of output. The first one is the force in all three axes acting on the scoop during the soil interaction, which can be directly compared

Fig. 18 The InSight scoop interacting with granular particles captured from three-dimensional X-ray computed tomography. The exact geometry of the scoop can be replicated in advanced DE Models. These methods can simulate different particle size distributions and particle shapes
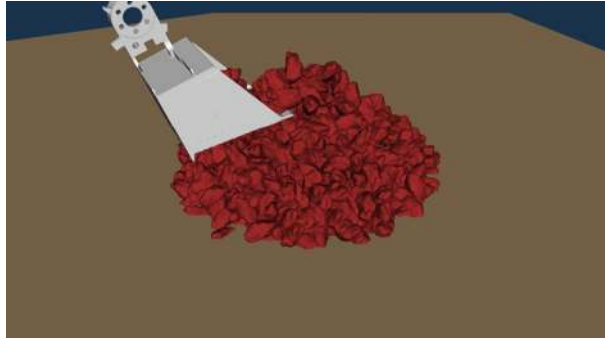
to the force acting on the IDA during operations. The second output is the redistribution of grains. Thus, trench depths, trench angles, and the angle of repose of piles can be calculated. In future work, more advanced DE Models (Kawamoto et al. 2016) will be utilized to model different particle shapes and the exact scoop geometry.

6 Discussion

The results of the geology and physical properties investigations will directly test many predictions of the surface and subsurface that have been made using remote sensing data during the landing site evaluation (Golombek et al. 2017). To first order, comparison of the surface seen from the lander is "ground truth" to the orbital data and interpretations. At the broadest level, orbital observations support a model in which basalts deposited during the Hesperian have developed an impact generated regolith 3–17 m thick that has been modified by eolian processes. The information developed from the geology and physical properties investigations can be used to test this model as well as specific characteristics of the surface, materials present and geologic processes that have modified and shaped or are shaping the surface.

The shallow subsurface model of the InSight landing site was developed from the onset diameter of rocky ejecta craters (Warner et al. 2017), observations of nearby scarps at Hephaestus Fossae (Golombek et al. 2017; Warner et al. 2017), and predictions of fragmentation theory based on crater counts and rock distributions (Golombek et al. 2017, 2018, Charalambous et al. 2017). Knapmeyer-Endrun et al. (2017, 2018) used seismic velocities measured in regolith simulants (e.g., Delage et al. 2017) as well as field measurements of soils on top of young basalt flows in the Cima volcanic field in the Mojave Desert, where tephra and eolian material grades into a rubble zone of basaltic clasts and then highly fractured rock (e.g., Wells et al. 1985). This produces a step wise rapid increase in seismic velocities, elastic properties and seismic attenuation, Q (Knapmeyer-Endrun et al. 2017; Delage et al. 2017). Warner et al. (2017) used the onset diameter of rocky ejecta craters, the depth to the inner crater in nested craters, and roll-offs in the size-frequency distribution of rocky and non-rocky ejecta craters to measure the thickness of the regolith (3–17 m) at the landing site. In addition, fragmentation theory constrained by measured crater counts and rock abundance has been used to simulate the thickness of the regolith at the InSight landing site (Golombek et al. 2017, Charalambous 2015, Charalambous et al. 2017). Finally, the regolith thickness expected from impact gardening of the surface has also been related to the cratering record on the Moon (Oberbeck and Quaide 1968) and Mars (Hartmann et al. 2001).

These predictions of regolith thickness and elastic and seismic properties of the subsurface can be tested by InSight. The physical properties investigation will constrain the subsurface structure of the landing site using the HP^3 by the penetration of the mole, SEIS monitoring during mole hammering and by passive SEIS monitoring (e.g., Rayleigh wave inversion and other methods). The thickness of the regolith estimated by rocky ejecta craters at the specific landing location, fragmentation theory and impact gardening can thus be compared with measurements made by InSight.

Surface materials at the landing site have been estimated from thermophysical properties and albedo in orbital remote sensing data (Golombek et al. 2017). Surface materials are expected to be dominated by very fine to fine sand that is either cohesionless or has very low cohesion (less than a few kPa). The albedo, dust cover index (Ruff and Christensen 2002), and variations in thermal inertia all suggest the surface has an optically thick but thermally thin coating of dust similar to dusty portions of the Gusev cratered plains. Although the InSight lander carries no imagers capable of resolving sand size grains, other techniques can be used. First, the HP^3 radiometer can determine the thermal inertia at the surface and compare it to that obtained from orbit as has been done by MER and MSL (Golombek et al. 2005; Fergason et al. 2006; Hamilton et al. 2014; Vasavada et al. 2017). From images of the radiometer spots, their surfaces can be imaged and thus related to the thermal inertia measurements. Specifically, the areal fraction of rocks in the spots can be determined and from the measured size-frequency distribution of the rocks, the thermal inertia of the rocky component can be estimated and separated from the thermal inertia of the fine component (Golombek et al. 2003b). The thermal inertia of the fine component can be related to the particle size for cohesionless material (Presley and Christensen 1997a, 1997b) and any cohesion via theory (Piqueux and Christensen 2009, 2011) or soil mechanics measurements of soils by the robotic arm. In addition, the elastic properties derived from SEIS and indentation experiments, can be related to simulant properties (e.g., Delage et al. 2017) to see if they are consistent.

Fragmentation theory developed by Charalambous (2015) applied to the InSight landing site based on rock abundances from orbit and surface rock counts from the Spirit and Phoenix landers (Golombek et al. 2017) can be extrapolated to sand size particles (Charalambous et al. 2017; Golombek et al. 2018), thus allowing a comparison with the observations by InSight. Specific objectives for testing fragmentation theory would be to count the rocks around the landing site in HiRISE and compare their distribution with those measured by InSight as has been done at VL1, VL2, MPF and PHX (Golombek et al. 2008b, 2012b; Heet et al. 2009). This would not only provide another example in the model's library, but it would also help quantify better the landing site's maturity index which controls the abundance of smaller particles. This improved maturity index would help in the re-estimation of mole's probability of success penetrating 3–5 m, together with seismic signals obtained from hitting rocks during the mole's progress, and the final penetration depth. The particle size of the soils inferred from the thermal inertia can also be used to better understand the relative contributions from fragmentation versus eolian activity (e.g., Golombek et al. 2018).

The surface at the InSight landing site likely has a thin coating of dust (Golombek et al. 2017) that will be dispersed by the lander retro-rockets as has been observed by Phoenix and MSL (Daubar et al. 2015; Seelos et al. 2014). The dust is expected to be redeposited from the atmosphere over time and the relative albedo increase can be measured in repeat HiRISE images (e.g., Daubar et al. 2016) and perhaps CaSSIS and CRISM at 5 m/pixel and 18 m/pixel resolution, respectively (e.g., Thomas et al. 2017; Seelos et al. 2014). Surface images can identify pockets of dust by their relatively bright reddish color that might be protected from dispersal by the retrorocket exhaust. Although

the imagers do not have individual color filters (Maki et al. 2018), spectra from the Bayer filter blue, green, and red pixels can be used to identify dusty surfaces by their bright reddish color. As a result, surface images can confirm the dusty surface expected in orbital data.

The smooth terrain that the InSight ellipse is mostly located on is expected to be relatively smooth and flat with few rocks. The slopes at several m and ∼100 m length scale were measured in orbital images and DEMs (Fergason et al. 2017; Beyer 2017; Golombek et al. 2017) and surface slopes around the lander from stereo images can be compared with those measured from orbit. Rock abundance is also expected to be low from measurement of shadows in HiRISE images, unless landing is near a rocky ejecta crater (Golombek et al. 2017). In either case, rock size-frequency distributions from HiRISE images of the surface can be compared with those from orbit (e.g., Golombek et al. 2008b, 2012b; Heet et al. 2009).

If rocks are relatively close to the lander, the texture, fabric and morphology of rocks can provide clues to the rock type (e.g., McSween et al. 1999). The color can be related to their surface visible spectra, with basalts expected to have a relatively low reflectance in the visible (and especially in the red for dust free surfaces, e.g., McSween et al. 2004). The morphometry (shape and roundness) of the rocks observed by the lander can also be related to the depositional and erosional processes that have acted on them (e.g., Garvin et al. 1981; Yingst et al. 2007, 2008, 2013; Craddock and Golombek 2016; Szabo et al. 2015). Finally, if a small vesicular volcanic rock is nearby the lander and can be pushed by the robotic arm, it might be possible to derive the rock's density and infer its composition (e.g., Thomson et al. 2008).

If landing were to occur close to a crater, the morphology and morphometry of the crater can be compared to that measured from orbit. In addition to rocky and non-rocky ejecta craters in a variety of degradational states (Warner et al. 2017; Sweeney et al. 2016), the most common craters at the landing site are secondary craters from Corinto, a fresh rayed crater about 600 km northeast of the landing site (Bloom et al. 2014), with distinct thermal rays that extend for over 2000 km. The thermal rays are composed of dense swarms of small secondaries and several thermal rays cross the landing ellipse (Golombek et al. 2017). Corinto secondary craters have shallow depth diameter ratios (∼0.05) with conical to parabolic shapes and bright ejecta. If InSight landed near a Corinto secondary its morphometry and morphology could be compared to that observed from orbit. If a small primary crater is in view of the lander, its morphometry can be compared to expectations for fresh impact craters in fragmented regolith (shallow depth/diameter and wall slopes, Stopar et al. 2017; Watters et al. 2015), similar to fresh craters at the Gusev cratered plains (Golombek et al. 2006a) and expectations at the InSight landing site (Sweeney et al. 2016, 2018). Finally, observations of small primary impacts (∼10 cm) can be related to the density of the atmosphere that the meteoroid survived without ablating completely to impact the surface (e.g., Paige et al. 2007).

Eolian bedforms on the smooth terrain are present around relatively fresh craters where sand size particles have been moved by the wind. Most of the bedforms appear similar to ripples and are bright in HiRISE images suggesting they are dust covered and thus not recently active. As the craters degrade and fill in, the number and size of the bedforms decrease, suggesting the bedforms transition into a soil unit with slight near-surface cohesion from possible cements left by thin films of water (e.g., Haskin et al. 2005; Hurowitz et al. 2006). As a result, cohesion might be expected in near surface soils of the smooth terrain away from craters. Any bedforms in view by the lander can be related to bedforms seen from orbit and the meteorology data recorded on the lander to compare with wind direction, speed and any changes through time.

7 Conclusions and Summary

Investigation of the geology and physical properties of the surface where InSight lands will be conducted by the color cameras, the HP^3 mole and radiometer, the seismometer, and the instrument deployment arm and scoop. The instrument deployment system includes two color cameras, one mounted on an instrument deployment arm that can acquire full color, stereo panoramas and high-resolution images of the surface including the crescent shaped instrument deployment workspace. The IDA has a scoop that can perform basic soil mechanics investigations from calibrated motor currents and surface indentations, scraping, trenching and piling. The HP^3 will measure the thermal conductivity at 50 cm intervals as the mole penetrates 3–5 m below the surface and the penetration rate depends on the soil density, cohesion and angle of internal friction, which can be analyzed by comparing results with laboratory experiments and numerical models. An infrared radiometer can measure the surface temperature of two surface spots to determine the thermal inertia, which can be related to particle size and/or cohesion. Stereo images of the radiometer spots can be used to separate the thermal inertia of the rocky component as well as the fine or soil component. SEIS monitoring of atmospheric disturbances, high-frequency surface waves, lander mechanical noise, cut-off frequency of impacts, as well as HP^3 mole hammering will be used to extract elastic physical properties, P- and S-wave velocities, seismic attenuation and their variations with depth via seismic exploration techniques. Meteorology instruments will measure pressure and wind speed and direction continuously and thus will record dust devils or wind vortices and peak winds that can be related to imaged dust devil tracks, eolian changes and threshold friction wind stress for grain motion on Mars. The geology and physical properties investigation are central to finding locations that are smooth, flat (< 15 °), rock free (no rocks > 3 cm high), and load bearing in the workspace where the instruments can be placed by the arm.

Geologic mapping in medium- and high-resolution orbital images indicates the InSight landing site in western Elysium Planitia, just north of the dichotomy boundary, is underlain by basaltic lava flows. Images show a diversity of morphologies, including flow fronts, lobate ridges, inflation plateaus, smooth and platy surface textures, and vents suggesting low viscosity flows erupted in the Early Hesperian. The plains surface was deformed by wrinkle ridges, which have been interpreted to be fault-propagation folds, in which slip on thrust faults at depth are accommodated by asymmetric folding in strong, but weakly bonded layered material (such as basalt flows) near the surface. Partially filled craters and the maximum thickness of strong basalt from rocky ejecta craters indicate the basalts are 200–300 m thick and are underlain by weak sediments. The lack of rocks in most fresh craters < 50 m diameter and concentric or nested craters argue for a surficial fragmented regolith 3–17 m thick. Exposures of relatively fine-grained regolith $\sim$10 m thick that grades with depth into coarse breccia overlying strong jointed bedrock in nearby Hephaestus Fossae in southern Utopia Planitia, suggests the regolith was built up by impacts in agreement with fragmentation theory constrained by the size-frequency distribution of craters and observed rock abundance in HiRISE images.

Investigation of the InSight landing site in remote sensing data during landing site selection indicates a smooth, flat surface with very low rock abundance sparsely punctuated by relatively fresh rocky ejecta craters as well as ubiquitous small secondary craters from Corinto crater $\sim$600 km to the north-northeast. Relatively homogeneous thermal inertia of the surface indicates it is dominated by fine to very fine sand that is either cohesionless or has very low cohesion with no difference in properties within a few tens of centimeters of the surface. The dust cover index, albedo and thermophysical properties indicate the surface is covered by an optically thick but thermally thin ($<$hundreds of µm) coating of dust.

Eolian bedforms are concentrated in the ejecta and interiors of fresh craters and relatively absent in the inter-crater smooth plains indicating sand organizes into bedforms soon after crater formation and rapidly migrate over the rims and into the interiors of the craters. Northwest trending dust devil tracks are common and the northeast orientation of bedforms inside craters and their concentration on the outer northwest margins of crater rims suggest formative winds from the northwest. These observations indicate the surface is shaped by impact and eolian processes, consistent with the estimated slow erosion and degradation rates of the rocky ejecta craters.

The geology investigation characterizes the geology of the InSight landing site and provides ground truth for orbital remote sensing data. Similar investigations for previous missions have established the basic geologic evolution of the local region, identified the geologic materials present, and quantified their areal coverage. The information gathered about the geology of the surface can be used to infer the geologic processes that have operated on it and the shallow subsurface structure. This will test specific predictions made using orbital remote sensing during landing site selection including: rock size-frequency distributions, surface slopes, thermal inertia and soil properties, and eolian features and activity. Continuous measurements of wind speed and direction offer a unique opportunity to correlate dust devils and high winds with eolian changes imaged at the surface and to determine the threshold friction wind stress for grain motion on Mars. The removal of dust by thrusters during landing will darken the surface and brightening with time can be determined using surface and orbital images. This brightening is expected from dust settling from the atmosphere, and that rate of dustfall can be compared with the amount of dust present in the atmosphere (from camera opacity measurements) and dust falling on the solar panels (from solar array energy).

Soil mechanics parameters and elastic constants of near surface materials will be determined from mole penetration and thermal conductivity measurements from the surface to 3–5 m depth, the measurement of seismic waves generated during mole hammering, passive monitoring of seismic waves, and soil mechanics experiments with the arm and scoop (indentations, scraping, trenching and piling). Calibrated motor currents of the arm and interactions of the scoop with the surface can be used to derive standard soil mechanics parameters such as the angle of repose or angle of internal friction from piles of soil created on the surface, cohesion from scraping and elastic properties (Young's and shear moduli) from indentations. The HP^3 mole penetration speed will be used to constrain the angle of internal friction and soil density using soil physics models and laboratory studies of simulants. SEIS passive monitoring of atmospheric disturbances, high-frequency surface waves, lander mechanical noise, and cut-off frequency of impacts can be used to estimate P- and S-wave velocities with depth in the shallow subsurface as well as regolith thickness and porosity. SEIS measurement of HP^3 mole hammering will be used to extract elastic physical properties, P- and S-wave velocities, seismic attenuation and their variations with depth via seismic exploration techniques. Combining these different techniques will yield soil mechanics parameters as well as seismic velocities and attenuation with depth that will reduce travel-time and amplitude errors of globally propagating seismic waves.

The results of the InSight geology and physical properties investigations will determine and test the presence and mechanical properties of the expected 3–17 m thick fragmented regolith built up on top of Hesperian lava flows by impact and eolian activity and determine its seismic properties for the seismic investigation of Mars' interior. Surface material properties characterized by the InSight lander can be compared to those expected from orbital remote sensing data at the landing site such as thermal inertia, particle size and cohesion, rock abundance, and dustiness. Geologic processes expected from orbital data that are important in shaping the surficial layer (impact and eolian) can be compared with that found

from the lander. These comparisons of the surface seen from the lander are "ground truth" to orbital remote sensing data and interpretations and are important for future landing site selection on Mars.

References

H. Abarca, R. Deen, G. Hollins, P. Zamani, O. Pariser, J. Maki, F. Ayoub, A. Tinio, N. Toole, S. Algermissen, T. Soliman, Y. Lu, M. Golombek, F. Calef III., K. Grimes, Image and data processing for InSight lander operations and science. Space Sci. Rev. (2018, this issue)

K.A. Alshibli, A. Hasan, Strength properties of JSC-1A lunar regolith simulant. J. Geotech. Geoenviron. Eng. **135**(5), 673–679 (2009)

R.E. Arvidson, R.C. Anderson, P. Bartlett, J.F. Bell III, D. Blaney, P.R. Christensen, P. Chu, L. Crumpler, K. Davis, B.L. Ehlmann, R. Fergason, M.P. Golombek et al., Localization and physical properties experiments conducted by Spirit at Gusev crater. Science **305**(5685), 821–824 (2004a). https://doi.org/10.1126/science.1099922

R.E. Arvidson, R.C. Anderson, P. Bartlett, J.F. Bell III, P.R. Christensen, P. Chu, K. Davis, B.L. Ehlmann, M.P. Golombek et al., Localization and physical properties experiments conducted by Opportunity at Meridiani Planum. Science **306**(5702), 1730–1733 (2004b). https://doi.org/10.1126/science.1104211

R. Arvidson, D. Adams, G. Bonfiglio, P. Christensen, S. Cull, M. Golombek, J. Guinn, E. Guinness, T. Heet, R. Kirk, A. Knudson, M. Malin, M. Mellon, A. McEwen, A. Mushkin, T. Parker, F. Seelos, K. Seelos, P. Smith, D. Spencer, T. Stein, L. Tamppari, Mars Exploration Program 2007 Phoenix landing site selection and characteristics. J. Geophys. Res., Planets **113**, E00A03 (2008). https://doi.org/10.1029/2007JE003021

R.E. Arvidson et al., Terrain physical properties derived from orbital data and the first 360 sols of Mars Science Laboratory Curiosity rover observations in Gale Crater. J. Geophys. Res., Planets **119**, 1322–1344 (2014). https://doi.org/10.1002/2013JE004605

J.H. Atkinson, G. Sallfors, Experimental determination of soil properties. General Report to Session 1, in *Proceedings of the 10th ECSMFE, Florence 3* (1991), pp. 915–956

F. Ayoub, J.P. Avouac, C.E. Newman, M.I. Richardson, A. Lucas, S. Leprince, N.T. Bridges, Threshold for sand mobility on Mars calibrated from seasonal variations of sand flux, in *Eighth International Conference on Mars*, Pasadena, CA, July 14–18, 2014 (Lunar and Planetary Institute, Houston, 2014). Abstract #1064

C. Bagaini, C. Barajas-Olalde, Assessment and compensation of inconsistent coupling conditions in point-receiver land seismic data. Geophys. Prospect. **55**, 39–48 (2007). https://doi.org/10.1111/j.1365-2478.2006.00606.x

R.A. Bagnold, *The Physics of Blown Sand and Desert Dunes* (Methuen, New York, 1941)

J.L. Bandfield, R.R. Ghent, A.R. Vasavada, D.A. Paige, S.J. Lawrence, M.S. Robinson, Lunar surface rock abundance and regolith fines temperatures derived from LRO Diviner Radiometer data. J. Geophys. Res., Planets **116**, 18 (2011). https://doi.org/10.1029/2011je003866

W.B. Banerdt et al., The InSight Mission. Space Sci. Rev. (2018, this issue)

D. Banfield et al., The Auxiliary Payload Sensor Suite on InSight. Space Sci. Rev. (2018, this issue)

A. Becker, C. Vrettos, Tests on the thermal conductivity of regolith quasi-analogues at different porosities, in *Earth and Space 2016, 15th ASCE International Conference on Engineering, Science, Construction and Operations in Challenging Environments* (2016)

R.A. Beyer, Meter-scale slopes of candidate InSight landings sites from point photoclinometry. Space Sci. Rev. **211**, 97–107 (2017). https://doi.org/10.1007/s11214-016-0287-7

A.B. Binder, R.E. Arvidson, E.A. Guinness et al., The geology of the Viking Lander 1 site. J. Geophys. Res. **82**, 4439–4451 (1977)

J.E. Bleacher, T.R. Orr, A.P. de Wet, J.R. Zimbelman, C.W. Hamilton, W.B. Garry, L.S. Crumpler, D.A. Williams, Plateaus and sinuous ridges as the fingerprints of lava flow inflation in the Eastern Tharsis Plains of Mars. J. Volcanol. Geotherm. Res. **342**, 29–46 (2017). https://doi.org/10.1016/j.jvolgeores.2017.03.025

C. Bloom, M. Golombek, N. Warner, N. Wigton, Size frequency distribution and ejection velocity of Corinto crater secondaries in Elysium Planitia, in *Eighth International Conference on Mars*, Pasadena, CA, July 14–18, 2014, (Lunar and Planetary Institute, Houston, 2014). Abstract #1289

N.T. Bridges, F. Ayoub, J-P. Avouac, S. Leprince, A. Lucas, S. Mattson, Earth-like sand fluxes on Mars. Nature **485**, 339–342 (2012)

N. Bridges, P. Geissler, S. Silvestro, M. Banks, Bedform migration on Mars: current results and future plans. Aeolian Res. **9**, 133–151 (2013)

W.D. Carrier, J.K. Mitchell, A. Mahmood, The relative density of lunar soil, in *Proc. Lunar Sci. Conf., 4th*, vol. 4 (1973), pp. 118–120

M.A. Carrigy, Experiments on the angles of repose of granular materials. Sedimentology **14**(3–4), 147–158 (1970)

D.C. Catling et al., A lava sea in the northern plains of Mars: circumpolar Hesperian oceans reconsidered, in *42nd Lunar and Planetary Science Conference* (Lunar and Planetary Institute, Houston, 2011). Abstract #2529

D.C. Catling et al., Does the Vastitas Borealis formation contain oceanic or volcanic deposits? in *Third Conference on Early Mars*, Lake Tahoe, NV, May 21–25, 2012 (Lunar and Planetary Institute, Houston, 2012). Abstract #7031

T.E. Chamberlain, H.L. Cole, R.G. Dutton, G.C. Greene, J.E. Tillman, Atmospheric measurements of Mars: the Viking meteorology experiment. Bull. Am. Meteorol. Soc. **57**, 1094–1104 (1976)

C. Charalambous, On the evolution of particle fragmentation with applications to planetary surfaces. Ph.D. Thesis (Imperial College, London, 2015)

C. Charalambous, W.T. Pike, M.P. Golombek, Estimating the grain size distribution of Mars based on fragmentation theory and observations, in *2017 Fall AGU Meeting*, 11–15 Dec., New Orleans, LA (2017). Abstract P41C-2843

M. Chojnacki, J.R. Johnson, J.E. Moersch, L.K. Fenton, T.I. Michaels, J.F. Bell III, Persistent aeolian activity at Endeavour crater, Meridiani Planum, Mars; new observations from orbit and the surface. Icarus **251**, 275–290 (2015)

P.R. Christensen, The spatial distribution of rocks on Mars. Icarus **68**, 217–238 (1986)

P.R. Christensen, H.J. Moore, The martian surface layer, in *MARS*, ed. by H.H. Kieffer, B.M. Jakosky, C.W. Snyder, M.S. Matthews (University of Arizona Press, Tucson, 1992), pp. 686–727

P.R. Christensen, B.M. Jakosky, H.H. Kieffer, M.C. Malin, H.Y. McSween Jr., K. Nealson, G.L. Mehall, S.H. Silverman, S. Ferry, M. Caplinger, M. Ravine, The Thermal Emission Imaging System (THEMIS) for the Mars 2001 Odyssey mission. Space Sci. Rev. **110**, 85–130 (2004)

P. Claudin, B. Andreotti, A scaling low for aeolian dunes on Mars, Venus, Earth and for subaqueous ripples. Earth Planet. Sci. **252**, 30–44 (2006)

J.F. Clinton, D. Giardini, P. Lognonné, B. Banerdt, M. van Driel, M. Drilleau, N. Murdoch, M. Panning, R. Garcia, D. Mimoun, M. Golombek, J. Tromp, R. Weber, M. Böse, S. Ceylan, I. Daubar, B. Kenda, A. Khan, L. Perrin, A. Spiga, Preparing for InSight: an invitation to participate in a blind test for Martian seismicity. Seismol. Res. Lett. **88**, 1290–1302 (2017). https://doi.org/10.1785/0220170094

J.F. Clinton et al., Marsquake Service—building a Martian seismicity catalogue for InSight. Space Sci. Rev. (2018, this issue)

S. Courrech du Pont, C. Narteau, X. Gao, Two modes for dune orientation. Geology **42**, 743–746 (2014)

R.A. Craddock, M.P. Golombek, Characteristics of terrestrial basaltic rock populations: implications for Mars lander and rover science and safety. Icarus **274**, 50–72 (2016). https://doi.org/10.1016/j.icarus.2016.02.042

I.J. Daubar, A.S. McEwen, M.P. Golombek, Albedo changes at Martian landing sites, in *46th Lunar and Planetary Science* (Lunar and Planetary Institute, Houston, 2015). Abstract #2225

I.J. Daubar, C.M. Dundas, S. Byrne, P. Geissler, G.D. Bart, A.S. McEwen, P.S. Russell, M. Chojnacki, M.P. Golombek, Changes in blast zone albedo patterns around new martian impact craters. Icarus **267**, 86–105 (2016). https://doi.org/10.1016/j.icarus.2015.11.032

I.J. Daubar et al., Impact-seismic investigations of the InSight mission. Space Sci. Rev. (2018, this issue)

P. Delage, F. Karakostas, A. Dhemaied, M. Belmokhtar, P. Lognonné, M. Golombek, E. De Laure, K. Hurst, J.-C. Dupla, S. Kedar, Y.J. Cui, B. Banerdt, An investigation of the mechanical properties of some Martian regolith simulants with respect to the surface properties at the InSight mission landing site. Space Sci. Rev. **211**, 191–213 (2017). https://doi.org/10.1007/s11214-017-0339-7

L. Drube et al., Magnetic and optical properties of airborne dust and settling rates of dust at the Phoenix landing site. J. Geophys. Res. **115**, E00E23 (2010). https://doi.org/10.1029/2009JE003419

C.S. Edwards, K.J. Nowicki, P.R. Christensen, J. Hill, N. Gorelick, K. Murray, Mosaicking of global planetary image datasets: 1. Techniques and data processing for Thermal Emission Imaging System (THEMIS) multi-spectral data. J. Geophys. Res. **116**, E10008 (2011). https://doi.org/10.1029/2010je003755

B.L. Ehlmann et al., Chemistry, mineralogy, and grain properties at Namib and high dunes, Bagnold dune field, Gale crater, Mars: a synthesis of curiosity rover observations. J. Geophys. Res., Planets **122**, 2510–2543 (2018). https://doi.org/10.1002/2017JE005267

L. Fayon et al., A numerical model of the SEIS leveling system transfer matrix and resonances: Application to SEIS rotational seismology and dynamic ground interaction. Space Sci. Rev. (2018, in review, this issue)

R.L. Fergason, P.R. Christensen, J.F. Bell III, M.P. Golombek, K.E. Herkenhoff, H.H. Kieffer, Physical properties of the Mars Exploration Rover landing sites as inferred from Mini-TES derived thermal inertia. J. Geophys. Res. **111**(E2), E02S21 (2006). https://doi.org/10.1029/2005JE002583

R. Fergason, R.L. Kirk, G. Cushing, D.M. Galuzska, M.P. Golombek, T.M. Hare, E. Howington-Kraus, D.M. Kipp, B.L. Redding, Analysis of local slopes at the InSight landing site on Mars. Space Sci. Rev. **211**, 109–133 (2017). https://doi.org/10.1007/s11214-016-0292-x

L. Fernandez-Cascales, A. Lucas, S. Rodriguez, X. Gao, A. Spiga, C. Narteau, First quantification of relationship between dune orientation and sediment availability, Olympia Undae, Mars. Earth Planet. Sci. Lett. **489**, 241–250 (2018). https://doi.org/10.1016/j.epsl.2018.03.001

W. Folkner, V. Dehant, S. Le Maistre, M. Yseboodt, A. Rivoldini, T. Van Hoolst, S.W. Asmar, M.P. Golombek, The Rotation and Interior Structure Experiment on the InSight Mission to Mars. Space Sci. Rev. (2018, this issue)

H.V. Frey, Impact constraints on, and a chronology for, major events in early Mars history. J. Geophys. Res. **111**, E08S91 (2006). https://doi.org/10.1029/2005JE002449

X. Gao, C. Narteau, O. Rozier, S. Courrech du Pont, Phase diagrams of dune shape and orientation depending on sand availability. Sci. Rep. **5**, 14677 (2015)

E. Gardin, P. Allemand, C. Quantin, S. Silvestro, C. Delacourt, Dune fields on Mars: recorders of a climate change? Planet. Space Sci. **60**, 314–321 (2012)

J.B. Garvin, P.J. Mouginis-Mark, J.W. Head, Characterization of rock populations on planetary surfaces: techniques and a preliminary analysis of Mars and Venus. Moon Planets **24**, 355–387 (1981)

J.B. Garvin, S.E.H. Sakamoto, C. Schnetzler, J.J. Frawley, Craters on Mars: global geometric properties from gridded MOLA topography, in *6th International Conference on Mars*, 20–25 July (California Institute of Technology, Pasadena, 2003). Abs. #3277

W. Goetz et al., Microscopy analysis of soils at the Phoenix landing site, Mars: classification of soil particles and description of their optical and magnetic properties. J. Geophys. Res. **115**, E00E22 (2010). https://doi.org/10.1029/2009JE003437

M.P. Golombek, N.T. Bridges, Erosion rates on Mars and implications for climate change: constraints from the Pathfinder landing site. J. Geophys. Res., Planets **105**(E1), 1841–1853 (2000). https://doi.org/10.1029/1999JE001043

M.P. Golombek, R.J. Phillips, Mars tectonics, in *Planetary Tectonics*, ed. by T.R. Watters, R.A. Schultz (Cambridge University Press, Cambridge, 2010), pp. 183–232. Chap. 5

M.P. Golombek, J.B. Plescia, B.J. Franklin, Faulting and folding in the formation of planetary wrinkle ridges, in *Proc. Lunar Planet. Sci. Conf*, vol. 21 (1991), pp. 679–693

M.P. Golombek, R.A. Cook, T. Economou, W.M. Folkner, A.F.C. Haldemann, P.H. Kallemeyn, J.M. Knudsen, R.M. Manning, H.J. Moore, T.J. Parker, R. Rieder, J.T. Schofield, P.H. Smith, R.M. Vaughan, Overview of the Mars Pathfinder mission and assessment of landing site predictions. Science **278**, 1743–1748 (1997a)

M.P. Golombek, R.A. Cook, H.J. Moore, T.J. Parker, Selection of the Mars Pathfinder landing site. J. Geophys. Res. **102**, 3967–3988 (1997b)

M.P. Golombek et al., Overview of the Mars Pathfinder mission: launch through landing, surface operations, data sets, and science results. J. Geophys. Res. **104**, 8523–8553 (1999a)

M.P. Golombek, H.J. Moore, A.F.C. Haldemann, T.J. Parker, J.T. Schofield, Assessment of Mars Pathfinder landing site predictions. J. Geophys. Res. **104**, 8585–8594 (1999b)

M.P. Golombek et al., Selection of the Mars Exploration Rover landing sites. J. Geophys. Res. **108**(E12), 8072 (2003a). https://doi.org/10.1029/2003JE002074

M.P. Golombek, A.F.C. Haldemann, N.K. Forsberg-Taylor, E.N. DiMaggio, R.D. Schroeder, B.M. Jakosky, M.T. Mellon, J.R. Matijevic, Rock size-frequency distributions on Mars and implications for Mars Exploration Rover landing safety and operations. J. Geophys. Res. **108**(E12), 8086 (2003b). https://doi.org/10.1029/2002JE002035

M.P. Golombek et al., Assessment of Mars Exploration Rover landing site predictions. Nature **436**, 44–48 (2005). https://doi.org/10.1038/nature03600

M.P. Golombek et al., Geology of the Gusev cratered plains from the Spirit rover traverse. J. Geophys. Res. **110**, E02S07 (2006a). https://doi.org/10.1029/2005JE002503

M.P. Golombek, J.A. Grant, L.S. Crumpler, R. Greeley, R.E. Arvidson, J.F. Bell III, C.M. Weitz, R. Sullivan, P.R. Christensen, L.A. Soderblom, S.W. Squyres, Erosion rates at the Mars Exploration Rover landing sites and long-term climate change on Mars. J. Geophys. Res., Planets **111**, E12S10 (2006b). https://doi.org/10.1029/2006JE002754

M.P. Golombek, A.F.C. Haldemann, R.A. Simpson, R.L. Fergason, N.E. Putzig, R.E. Arvidson, J.F. Bell III, M.T. Mellon, Martian surface properties from joint analysis of orbital, Earth-based, and surface observations, in *The Martian Surface: Composition, Mineralogy and Physical Properties*, ed. by J.F. Bell III (Cambridge University Press, Cambridge, 2008a), pp. 468–497. Chap. 21

M.P. Golombek et al., Size-frequency distributions of rocks on the northern plains of Mars with special reference to Phoenix landing surfaces. J. Geophys. Res. **113**, E00A09 (2008b). https://doi.org/10.1029/2007JE003065

M. Golombek, K. Robinson, A. McEwen, N. Bridges, B. Ivanov, L. Tornabene, R. Sullivan, Constraints on ripple migration at Meridiani Planum from Opportunity and HiRISE observations of fresh craters. J. Geophys. Res. **115**, E00F08 (2010). https://doi.org/10.1029/2010JE003628

M. Golombek, J. Grant, D.D. Kipp, A. Vasavada, R. Kirk, R. Fergason, P. Bellutta, F. Calef, K. Larsen, Y. Katayama, A. Huertas, R. Beyer, A. Chen, T. Parker, B. Pollard, S. Lee, R. Hoover, H. Sladek, J. Grotzinger, R. Welch, E. Noe Dobrea, J. Michalski, M.M. Watkins, Selection of the Mars Science Laboratory landing site. Space Sci. Rev. **170**, 641–737 (2012a). https://doi.org/10.1007/s11214-012-9916-y

M. Golombek, A. Huertas, D. Kipp, F. Calef, Detection and characterization of rocks and rock size-frequency distributions at the final four Mars Science Laboratory landing sites. Mars **7**, 1–22 (2012b). https://doi.org/10.1555/mars.2012.0001

M.P. Golombek, N.H. Warner, V. Ganti, M.P. Lamb, T.J. Parker, R.L. Fergason, R. Sullivan, Small crater modification on Meridiani Planum and implications for erosion rates and climate change on Mars. J. Geophys. Res., Planets **119**, 2522–2547 (2014). https://doi.org/10.1002/2014JE004658

M. Golombek, D. Kipp, N. Warner, I.J. Daubar, R. Fergason, R. Kirk, R. Beyer, A. Huertas, S. Piqueux, N.E. Putzig, B.A. Campbell, G.A. Morgan, C. Charalambous, W.T. Pike, K. Gwinner, F. Calef, D. Kass, M. Mischna, J. Ashley, C. Bloom, N. Wigton, T. Hare, C. Schwartz, H. Gengl, L. Redmond, M. Trautman, J. Sweeney, C. Grima, I.B. Smith, E. Sklyanskiy, M. Lisano, J. Benardini, S. Smrekar, P. Lognonné, W.B. Banerdt, Selection of the InSight landing site. Space Sci. Rev. **211**, 5–95 (2017). https://doi.org/10.1007/s11214-016-0321-9

M.P. Golombek, C. Charalambous, W.T. Pike, R. Sullivan, The origin of sand on Mars, in *49th Lunar and Planetary Science* (Lunar and Planetary Institute, Houston, 2018). Abstract #2319

J. Gomez-Elvira, C. Armiens, L. Castaner, M. Dominguez, M. Genzer, F. Gomez, R. Haberle, A.-M. Harri, V. Jimenez, H. Kahanpaa, A. Kowalski, A. Lepinette, J. Martin, J. Martinez-Frias, I. McEwan, L. Mora, J. Moreno et al., REMS: the environmental sensor suite for the Mars Science Laboratory Rover. Space Sci. Rev. **170**, 583–640 (2012)

S. Goossens, T.J. Sabaka, A. Genova, E. Mazarico, J.B. Nicholas, G.A. Neumann, Evidence for a low bulk crustal density for Mars from gravity and topography. Geophys. Res. Lett. **44**, 7686–7694 (2017). https://doi.org/10.1002/2017GL074172

R. Greeley, J.D. Iversen, *Wind as a Geological Process on Earth, Mars, Venus and Titan*. Cambridge Planetary Science Series, vol. 4 (Cambridge Univ. Press, Cambridge, 1985)

R. Greeley, A. Skypeck, J.B. Pollack, Martian aeolian features and deposits—comparisons with general circulation model results. J. Geophys. Res. **98**, 3183–3196 (1993)

R. Greeley, N.T. Bridges, R.O. Kuzmin, J.E. Laity, Terrestrial analogs to wind-related features at the Viking and Pathfinder landing sites on Mars. J. Geophys. Res. **107**(E1), E5005 (2002)

T.K.P. Gregg, Patterns and processes: Subaerial lava flow morphologies: a review. J. Volcanol. Geotherm. Res. **342**, 3–12 (2017). https://doi.org/10.1016/j.jvolgeores.2017.04.022

M. Grott, Thermal disturbances caused by lander shadowing and the measurability of the martian planetary heat flow. Planet. Space Sci. **57**, 71–77 (2009)

M. Grott, J. Helbert, R. Nadalini, Thermal structure of Martian soil and the measurability of the planetary heat flow. J. Geophys. Res. **112**, E09004 (2007)

T.V. Gudkova, P. Lognonné, J. Gagnepain-Beyneix, Large impacts detected by the Apollo seismometers: impactor mass and source cutoff frequency estimation. Icarus **211**, 1049–1065 (2011)

T. Gudkova, P. Lognonné, K. Miljkovic, J. Gagnepain-Beyneix, Impact cut-off frequency-momentum scaling law inverted from Apollo seismic data. Earth Planet. Sci. Lett. **427**, 57–65 (2015). https://doi.org/10.1016/j.epsl.2015.06.037

V.E. Hamilton, A.R. Vasavada, E. Sebastián, M. de la Torre Juárez, M. Ramos et al., Observations and preliminary science results from the first 100 sols of MSL Rover Environmental Monitoring Station ground temperature sensor measurements at Gale Crater. J. Geophys. Res., Planets **119**, 745–770 (2014). https://doi.org/10.1002/2013JE004520

M. Hamm, M. Grott, E. Kührt et al., A method to derive surface thermophysical properties of asteroid (162173) Ryugu (1999JU3) from in-situ surface brightness temperature measurements. Planet. Space Sci. (2018, submitted)

H. Hansen-Goos, M. Grott, R. Lichtenheld et al., Predicted penetration performance of the InSight HP3 mole, in *Lunar and Planetary Science Conference*, 45 (2014). Abstract #1325

B.A. Hardage, Vertical seismic profiling: principles, in *Handbook of Geophysical Exploration*. Seismic Exploration, vol. 14 (Pergamon, Elmsford, 2000)

W.K. Hartmann, A.J. de la Casa, M. Berman, D.D. Ryan, E. Martian, Cratering 7: the role of impact gardening. Icarus **149**, 37–53 (2001)

L.A. Haskin et al., Water alteration of rocks and soils on Mars at the Spirit rover site in Gusev crater. Nature **436**, 66–69 (2005). https://doi.org/10.1038/nature03640

R.K. Hayward, K.F. Mullins, L.K. Fenton, T.M. Hare, T.N. Titus, M.C. Bourke, A. Colaprete, P.R. Christensen, Mars Global Digital Dune Database and initial science results. J. Geophys. Res. **112**, E11007 (2007). https://doi.org/10.1029/2007JE002943

J.W. Head, M.A. Kreslavsky, S. Pratt, Northern lowlands of Mars: evidence for widespread volcanic flooding and tectonic deformation in the Hesperian period. J. Geophys. Res. **107**(E1), 1–29 (2002). https://doi.org/10.1029/2000JE001445

E. Hébrard, C. Listowski, P. Coll, B. Marticorena, G. Bergametti, A. Määttänen, F. Montmessin, F. Forget, An aerodynamic roughness length map derived from extended Martian rock abundance data. J. Geophys. Res. **117**, E04008 (2012). https://doi.org/10.1029/2011JE003942

T.L. Heet, R.E. Arvidson, S.C. Cull, M.T. Mellon, K.D. Seelos, Geomorphic and geologic settings of the Phoenix lander mission landing site. J. Geophys. Res. **114**, E00E04 (2009). https://doi.org/10.1029/2009JE003416

K.E. Herkenhoff, M.P. Golombek, E.A. Guiness, J.B. Johnson, A. Kusack, L. Richter, R.J. Sullivan, S. Gorevan, In situ observations of the physical properties of the martian surface, in *The Martian Surface: Composition, Mineralogy and Physical Properties*, ed. by J.F. Bell III (Cambridge University Press, Cambridge, 2008), pp. 451–467. Chap. 20

M. Hobiger, N. Le Bihan, C. Cornou, P.-Y. Bard, Multicomponent signal processing for Rayleigh wave ellipticity estimation. IEEE Signal Process. Mag. **29**, 29–39 (2012). https://doi.org/10.1109/MSP.2012.2184969

R.D. Holtz, W.D. Kovacs, *An Introduction to Geotechnical Engineering* (Prentice Hall, New York, 1981)

K. Hon, J. Kauahikaua, R. Denlinger, K. Mackay, Emplacement and inflation of pahoehoe sheet flows: observations and measurements of active lava flows on Kilauea Volcano, Hawaii. Geol. Soc. Am. Bull. **106**(3), 351–370 (1994)

K.C. Horstman, H.J. Melosh, Drainage pits in cohesionless materials: implications for the surface of Phobos. J. Geophys. Res. **94**(B9), 12433–12441 (1989)

C.B. Hundal, M.P. Golombek, I.J. Daubar, Chronology of fresh rayed craters in Elysium Planitia, Mars, in *48th Lunar Planet. Sci. Conf.* (2017). Abstract 1726

J.A. Hurowitz, S.M. McLennan, N.J. Tosca, R.E. Arvidson, J.R. Michalski, D.W. Ming, C. Schroder, S.W. Squyres, In situ and experimental evidence for acidic weathering of rocks and soils on Mars. J. Geophys. Res. **111**, E02S19 (2006). https://doi.org/10.1029/2005JE002515

B.M. Jakosky, P.R. Christensen, Global duricrust on Mars: analysis of remote sensing data. J. Geophys. Res. **91**(B3), 3547–3560 (1986)

R. Kawamoto et al., Level set discrete element method for three-dimensional computations with triaxial case study. Journal of the Mechanics and Physics of Solids **91**, 1–13 (2016)

S. Kedar, J. Andrade, B. Banerdt, P. Delage, M. Golombek, M. Grott, T. Hudson, A. Kiely, M. Knappmeyer, B. Knapmeyer-Endrun, C. Krause, T. Kawamura, P. Lognonne, T. Pike, Y. Ruan, T. Spohn, N. Teanby, J. Tromp, J. Wookey, Analysis of regolith properties using seismic signals generated by InSight's HP^3 penetrator. Space Sci. Rev. **211**, 315–337 (2017). https://doi.org/10.1007/s11214-017-0391-3

B. Kenda, P. Lognonné, A. Spiga, T. Kawamura, S. Kedar, W.B. Banerdt, R. Lorenz, D. Banfield, M. Golombek, Modeling of ground deformation and shallow surface waves generated by Martian dust devils and perspectives for near-surface structure inversion. Space Sci. Rev. **211**, 501–524 (2017). https://doi.org/10.1007/s11214-017-0378-0

H.H. Kieffer, Thermal model for analysis of Mars infrared mapping. J. Geophys. Res., Planets **118**, 451470 (2013)

B. Knapmeyer-Endrun, M. Golombek, M. Ohrnberger, Rayleigh wave ellipticity modeling and inversion for shallow structure at the proposed InSight landing site in Elysium Planitia. Space Sci. Rev. **211**, 339–382 (2017). https://doi.org/10.1007/s11214-016-0300-1

B. Knapmeyer-Endrun, N. Murdoch, B. Kenda, M.P. Golombek, M. Knapmeyer, L. Witte, N. Verdier, S. Kedar, P. Lognonné, W.B. Banerdt, Influence of body waves, instrumentation resonances, and prior assumptions on Rayleigh wave ellipticity inversion for shallow structure at the InSight landing site. Space Sci. Rev. (2018, this issue)

N.I. Kömle, J. Poganski, G. Kargl, J. Grygorczuk, Pile driving models for the evaluation of soil penetration resistance measurements from planetary subsurface probes. Planet. Space Sci. **109–110**, 135–148 (2015)

A.S. Konopliv, S.W. Asmar, W.M. Folkner, Ö. Karatekin, D.C. Nunes, S.E. Smrekar, C.F. Yoder, M.T. Zuber, Mars high resolution gravity fields from MRO, Mars seasonal gravity, and other dynamical parameters. Icarus **211**, 401–428 (2011)

A.S. Konopliv, R.S. Park, W.M. Folkner, An improved JPL Mars gravity field and orientation from Mars orbiter and lander tracking data. Icarus **274**, 253–260 (2016). https://doi.org/10.1016/j.icarus.2016.02.052

L. Lancelot, I. Shahrour, M. Al Mahmoud, Comportement du sable d'Hostun sous faibles contraintes. Rev. Fr. Géotech. **74**, 63–74 (1996)

G.A. Landis, P.P. Jenkins, Measurement of the settling rate of atmospheric dust on Mars by the MAE instrument on Mars Pathfinder. J. Geophys. Res. **105**, 1855–1857 (2000)

K.L. Lee, H.B. Seed, Drained strength characteristics of drained sands. J. Soil Mech. Found. Div. **SM6**, 117–141 (1967)

M.T. Lemmon et al., Atmospheric imaging results from the Mars Exploration Rovers: Spirit and Opportunity. Science **306**, 1753–1756 (2004). https://doi.org/10.1126/science.1104474

R. Lichtenheldt, A novel systematic method to estimate the contact parameters of particles in discrete element simulations of soil, in *Particle-Based Methods IV* (2015), pp. 430–441. ISBN 978-84-944244-7-2

R. Lichtenheldt, *Lokomotorische Interaktion planetarer Explorationssysteme mit weichen Sandböden* (Verlag Dr. Hut, Munich, 2016). ISBN 978-3-8439-2704-8

R. Lichtenheldt, Covering shock waves on Mars induced by InSight's HP3-MOLE—efficient co-simulation using DEM and multi-domain dynamics, in *Coupled Problems 2017* (Artes Gráficas Torres S.L., Huelva, 2017). ISBN 978-84-943928-3-2

R. Lichtenheldt, O. Krömer, Soil modeling for InSight's HP3-Mole: from highly accurate particle-based towards fast empirical models, in *ASCE Earth and Space Conference* (2016)

R. Lichtenheldt, B. Schäfer, O. Krömer, Hammering beneath the surface of Mars—modeling and simulation of the impact-driven locomotion of the HP3-Mole by coupling enhanced multi-body dynamics and discrete element method. Shaping the future by engineering, in *58th Ilmenau Scientific Colloquium, IWK* (2014). urn:nbn:de:gbv:ilm1-2014iwk-155:2

P. Lognonné et al., SEIS: The Seismic Experiment for Internal Structure of InSight. Space Sci. Rev. (2018, this issue)

R. Lorenz, D. Christie, Dust devil signatures in infrasound records of the International Monitoring System. Geophys. Res. Lett. **42**, 2009–2014 (2015). https://doi.org/10.1002/2015GL063237

R.D. Lorenz, D. Reiss, Solar panel clearing events, dust devil tracks, and in-situ vortex detections on Mars. Icarus **248**, 162–164 (2015)

R. Lorenz, S. Kedar, N. Murdoch, P. Lognonné, T. Kawamura, D. Mimoun, W.B. Banerdt, Seismometer detection of dust devil vortices by ground tilt. Bull. Seismol. Soc. Am. **105**, 3015–3023 (2015)

P. Lü, C. Narteau, Z. Dong, O. Rozier, S. Courrech du Pont, Unravelling raked linear dunes to explain the coexistence of bedforms in complex dune fields. Nat. Commun. **8**, 14239 (2017)

A. Lucas, C. Narteau, S. Rodriguez, O. Rozier, Y. Callot, A. Garcia, S. Courrech du Pont, Sediment flux from the morphodynamics of elongating linear dunes. Geology **43**, 1027–1030 (2015)

J.N. Maki, J.J. Lorre, P.H. Smith, R.D. Brandt, D.J. Steinwand, The color of Mars: measurements from the Pathfinder landing site. J. Geophys. Res., Planets **104**(E4), 8781–8794 (1999). https://doi.org/10.1029/98JE01767

J.N. Maki, J.F. Bell, K.E. Herkenhoff, S.W. Squyres, A. Kiely, M. Klimesh, M. Schwochert, T. Litwin, R. Willson, A. Johnson, M. Maimone, E. Baumgartner, A. Collins, M. Wadsworth, S.T. Elliot, A. Dingizian, D. Brown, E.C. Hagerott, L. Scherr, R. Deen, D. Alexander, J. Lorre, The Mars Exploration Rover Engineering Cameras. J. Geophys. Res. **108**(E12), 8071 (2003). https://doi.org/10.1029/2003JE002077

J. Maki, D. Thiessen, A. Pourangi, P. Kobzeff, T. Litwin, L. Scherr, S. Elliott, A. Dingizian, M. Maimone, The Mars Science Laboratory Engineering Cameras. Space Sci. Rev. **170**, 77–93 (2012). https://doi.org/10.1007/s11214-012-9882-4

J.N. Maki, M. Golombek, R. Deen, H. Abarca, C. Sorice, T. Goodsall, M. Lemmon, A. Trebi-Ollennu, B. Banerdt, The color cameras on the InSight lander. Space Sci. Rev. (2018, this issue)

N. Mangold, P. Allemand, P.G. Thomas, G. Vidal, Chronology of compressional deformation on Mars: evidence for a single and global origin. Planet. Space Sci. **48**, 1201–1211 (2000)

J.P. Marshall, T.L. Hudson, J.E. Andrade, Experimental investigation of InSight HP[3] mole interaction with Martian regolith simulant. Quasi-static and dynamic penetration testing. Space Sci. Rev. **211**, 1–4, 239–258 (2017)

A.S. McEwen, L.L. Tornabene, H. Team, E.M. Eliason, J.W. Bergstrom, N.T. Bridges, C.J. Hansen, W.A. Delamere, J.A. Grant, V.C. Gulick, K.E. Herkenhoff, L. Keszthelyi, R.L. Kirk, M.T. Mellon, S.W. Squyres, N. Thomas, C.M. Weitz, Mars Reconnaissance Orbiter's High-Resolution Imaging Science Experiment (HiRISE). J. Geophys. Res. **112**, E05S02 (2007). https://doi.org/10.1029/2005JE002605

G.E. McGill, A.M. Dimitriou, Origin of the Martian global dichotomy by crustal thinning in the Late Noachian or Early Hesperian. J. Geophys. Res. **95**, 12,595–12,605 (1990)

I.O. McGlynn, C.M. Fedo, H.Y. McSween Jr., Origin of basaltic soils at Gusev crater, Mars, by aeolian modification of impact-generated sediment. J. Geophys. Res. **116**, E00F22 (2011). https://doi.org/10.1029/2010JE003712

D.S. McKay, J.L. Carter, W.W. Boles, C. Allen, J. Allton, *JSC-1: A Lunar Soil Simulant. Engineering, Construction, and Operations in Space IV* (Am. Soc. Civil Engineers, Reston, 1994), pp. 857–866

H.Y. McSween Jr., S.L. Murchie, J.A. Crisp, N.T. Bridges, R.C. Anderson, J.F. Bell III, D.T. Britt, J. Brückner, G. Dreibus, T. Economou, A. Ghosh, M.P. Golombek, J.P. Greenwood, J.R. Johnson, H.J. Moore, R.V. Morris, T.J. Parker, R. Rieder, R. Singer, H. Wänke, Chemical, multispectral, and textural constraints on the composition and origin of rocks at the Mars Pathfinder landing site. J. Geophys. Res. **104**, 8679–8715 (1999)

H.Y. McSween et al., Basaltic rocks analyzed by the Spirit rover in Gusev crater. Science **305**, 842–845 (2004)

M. Mehta, N.O. Rennó, J. Marshall, M. Rob Grover, A. Sengupta, N.A. Rusche, J.F. Kok, R.E. Arvidson, W.J. Markiewicz, M.T. Lemmon, P.H. Smith, Explosive erosion during the Phoenix landing exposes subsurface water on Mars. Icarus **211**, 172–194 (2011). https://doi.org/10.1016/j.icarus.2010.10.003

M. Mehta, A. Sengupta, N.O. Rennó, J.W. Van Norman, P.G. Huseman, D.S. Gulick, M. Pokora, Thruster plume surface interactions: applications for spacecraft landings on planetary bodies. AIAA J. **51**, 2800–2818 (2013). https://doi.org/10.2514/1.J052408

M.T. Mellon, B.M. Jakosky, H.H. Kieffer, P.R. Christensen, High-resolution thermal inertia mapping from the Mars Global Surveyor Thermal Emission Spectrometer. Icarus **148**, 437–455 (2000)

M.T. Mellon, R.L. Fergason, N.E. Putzig, The thermal inertia of the surface of Mars, in *The Martian Surface: Composition, Mineralogy, and Physical Properties*, ed. by J.F. Bell III (Cambridge University Press, Cambridge, 2008)

H.J. Melosh, *Impact Cratering: A Geologic Process* (Oxford University Press, London, 1989)

D. Mimoun, N. Murdoch, P. Lognonné, K. Hurst, W.T. Pike, J. Hurley, T. Nébut, W.B. Banerdt (SEIS Team), The noise model of the SEIS seismometer of the InSight mission to Mars. Space Sci. Rev. **211**, 383–428 (2017). https://doi.org/10.1007/s11214-017-0409-x

M.E. Minitti, L.C. Kah, R.A. Yingst, K.S. Edgett, R.C. Anderson, L.W. Beegle, J.L. Carsten, R.G. Deen, W. Goetz, C. Hardgrove, D.E. Harker, MAHLI at the Rocknest sand shadow: science and science-enabling activities. J. Geophys. Res., Planets **118**(11), 2338–2360 (2013)

S. Monin, A. Obukhov, Basic laws of turbulent mixing in the ground layer of the atmosphere. Tr. Akad. Nauk SSSR Geofiz. Inst. **24**, 163–187 (1954)

H.J. Moore, R.E. Hutton, G.D. Clow, C.R. Spitzer, Physical properties of the surface materials of the Viking landing sites on Mars. U. S. Geol. Surv. Prof. Pap. **1389**, 222pp., 2plates (1987)

H.J. Moore, D. Bickler, J. Crisp et al., Soil-like deposits observed by Sojourner, the Pathfinder rover. J. Geophys. Res. **104**, 8729–8746 (1999)

J.E. Moores, M.T. Lemmon, H. Kahanpää, S.C. Rafkin, R. Francis, J. Pla-Garcia, K. Bean, R. Haberle, C. Newman, M. Mischna, A.R. Vasavada, Observational evidence of a suppressed planetary boundary layer in northern Gale Crater, Mars as seen by the Navcam instrument onboard the Mars Science Laboratory rover. Icarus **249**, 129–142 (2015)

P. Morgan, M. Grott, M. Golombek, P. Delage, B. Knapmeyer-Endrun, S. Piqueux, I.J. Daubar, C. Charalambous, T. Pike, N. Müller, A. Hagermann, M. Siegler, R. Lichtenheldt, N. Teanby, S. Kedar, A pre-landing assessment of regolith properties at the InSight landing site. Space Sci. Rev. (2018, this issue)

K. Mueller, M.P. Golombek, Compressional structures on Mars. Annu. Rev. Earth Planet. Sci. **32**, 435–464 (2004). https://doi.org/10.1146/annurev.earth.32.101802.120553

N. Murdoch, B. Kenda, T. Kawamura, A. Spiga, P. Lognonné, D. Mimoun, W.B. Banerdt, Estimations of the seismic pressure noise on Mars determined from Large Eddy Simulations and demonstration of pressure decorrelation techniques for the Insight mission. Space Sci. Rev. **211**, 457–483 (2017a). https://doi.org/10.1007/s11214-017-0343-y

N. Murdoch, D. Mimoun, R.F. Garcia, W. Rapin, T. Kawamura, P. Lognonné, Evaluating the wind-induced mechanical noise on the InSight seismometers. Space Sci. Rev. **211**, 419–455 (2017b). https://doi.org/10.1007/s11214-016-0311-y

T.A. Mutch, R.E. Arvidson, A.B. Binder, E.A. Guinness, E.C. Morris, The geology of the Viking Lander 2 site. J. Geophys. Res. **82**, 4452–4467 (1977)

G. Neugebauer, G. Munch, H. Kieffer, J.S.C. Chase, E. Miner, Mariner 1969 infrared radiometer results: temperatures and thermal properties of the martian surface. Astron. J. **76**, 719–728 (1971)

S.A. Nowicki, P.R. Christensen, Rock abundance on Mars from the Thermal Emission Spectrometer. J. Geophys. Res. **112**, E05007 (2007). https://doi.org/10.1029/2006JE002798

V.R. Oberbeck, W.L. Quaide, Genetic implications of lunar regolith thickness variations. Icarus **9**, 446–465 (1968)

L. Ojha, S.E. Smrekar, D. Nunes, Geophysical characterization of Elysium Planitia: Implications for the InSight Mission (2018, in preparation)

D.A. Paige, M.P. Golombek, J.N. Maki, T.J. Parker, L.S. Crumpler, J.A. Grant, J.P. Williams, MER small crater statistics: evidence against recent quasi-periodic climate variations, in *The Seventh International Conference on Mars*, Pasadena, CA, July 9–13, 2007 (Lunar and Planetary Institute, Houston, 2007). Abstract #3392 (CD-ROM)

L. Pan, C. Quantin, Regional geological context of the InSight Landing Site from mineralogy and stratigraphy. in *49th Lunar and Planetary Science* (Lunar and Planetary Institute, Houston, 2018). Abstract #1918

M.P. Panning, P. Lognonne, W.B. Banerdt, R. Garcia, M. Golombek, S. Kedar, B. Knapmeyer-Endrun, A. Mocquet, N.A. Teanby, J. Tromp, R. Weber, E. Beucler, J.-F. Blanchette-Guertin, E. Bozdag, M. Drilleau, T. Gudkova et al., Planned products of the Mars Structure Service for the InSight mission to Mars. Space Sci. Rev. **211**, 611–650 (2017). https://doi.org/10.1007/s11214-016-0317-5

G.H. Peters, W. Abbey, G.H. Bearman, G.S. Mungas, J.A. Smith, R.C. Anderson, S. Douglas, L.W. Beegle, Mojave Mars simulant—characterization of a new geologic Mars analog. Icarus **197**, 470–479 (2008). https://doi.org/10.1016/j.icarus.2008.05.004

G.M. Pharr, W.C. Oliver, F.R. Brotzen, On the generality of the relationship among contact stiffness, contact area, and elastic modulus during indentation. J. Mater. Res. **7**(3), 613–617 (1992)

R.J. Pike, Depth/diameter relations of fresh lunar craters: revision from spacecraft data. Geophys. Res. Lett. **1**, 291–294 (1974). https://doi.org/10.1029/GL001i007p00291

S. Piqueux, P.R. Christensen, A model of thermal conductivity for planetary soils: 2. Theory for cemented soils. J. Geophys. Res. **114**, E09006 (2009). https://doi.org/10.1029/2008je003309

S. Piqueux, P.R. Christensen, Temperature-dependent thermal inertia of homogeneous Martian regolith. J. Geophys. Res. **116**, E07004 (2011). https://doi.org/10.1029/2011je003805

T. Platz, G. Michael, K.L. Tanaka, J.A. Skinner Jr., C.M. Fortezzo, Crater-based dating of geological units on Mars: methods and application for the new global geological map. Icarus **225**, 806–827 (2013). https://doi.org/10.1016/j.icarus.2013.04.021

D.H. Plemmons, M. Mehta, B.C. Clark, S.P. Kounaves, L.L. Peach, N.O. Rennó, L.K. Tamppari, S.M.M. Young, Effects of the Phoenix Lander descent thruster plume on the Martian surface. J. Geophys. Res. **113**, E00A11 (2008). https://doi.org/10.1029/2007JE003059

A.-C. Plesa, M. Grott, M.T. Lemmon et al., Interannual perturbations of the Martian surface heat flow by atmospheric dust opacity variations. J. Geophys. Res., Planets **121**, 2166–2175 (2016)

J. Poganski, N.I. Kömle, G. Kargl et al., Extended pile driving model to predict the penetration of the Insight/HP^3 Mole into the martian soil. Space Sci. Rev. **211**, 1–4, 237–237 (2017a)

J. Poganski et al., DEM modelling of a dynamic penetration process on Mars as a part of the NASA InSight Mission. Proc. Eng. **175**, 43–50 (2017b)

H.-G. Poulos, E.-H. Davis, *Elastic Solutions for Soil and Rock Mechanics* (Wiley, New York, 1974)

B.A. Preblich, A.S. McEwen, D.M. Studer, Mapping rays and secondary craters from Martian crater Zunil. J. Geophys. Res., Planets **112**, E05006 (2007). https://doi.org/10.1029/2006JE002817

M.A. Presley, P.R. Christensen, Thermal conductivity measurements of particulate materials, Part I: A review. J. Geophys. Res. **102**, 6535–6549 (1997a)

M.A. Presley, P.R. Christensen, Thermal conductivity measurements of particulate materials, Part II: Results. J. Geophys. Res. **102**, 6551–6566 (1997b)

M.A. Presley, P.R. Christensen, The effect of bulk density and particle size sorting on the thermal conductivity of particulate materials under Martian atmospheric pressures. J. Geophys. Res. **102**(E4), 9221–9229 (1997c)

M.A. Presley, R.A. Craddock, Thermal conductivity measurements of particulate materials: 3. Natural samples and mixtures of particle sizes. J. Geophys. Res. **111**, E09013 (2006)

N.E. Putzig, M.T. Mellon, Apparent thermal inertia and the surface heterogeneity of Mars. Icarus **191**(1), 68–94 (2007). https://doi.org/10.1016/j.icarus.2007.1005.1013

F. Reiser, C. Schmelzbach, D. Sollberger, H. Maurer, S.A. Greenhalgh, S. Planke, F. Kästner, Ó. Flóvenz, R. Giese, S. Halldórsdóttir, G. Hersir, Imaging the high-temperature geothermal field at Krafla using vertical seismic profiling. J. Volcanol. Geotherm. Res. (2018, submitted)

D. Reiss, R.D. Lorenz, Dust devil track survey at Elysium Planitia, Mars: implications for the InSight landing sites. Icarus **266**, 315–330 (2016)

D.M. Rubin, R.E. Hunter, Bedform alignment in directionally varying flows. Science **237**, 276–278 (1987)

S. Ruff, P.R. Christensen, Bright and dark regions on Mars: particle size and mineralogical characteristics based on Thermal Emission Spectrometer data. J. Geophys. Res. **107**(E12), 5127 (2002). https://doi.org/10.1029/2001JE001580

K.D. Runyon, N.T. Bridges, F. Ayoub, C.E. Newman, J.J. Quade, An integrated model for dune morphology and sand fluxes on Mars. Earth Planet. Sci. Lett. **457**, 204–212 (2017)

C. Schmelzbach, A.G. Green, H. Horstmeyer, Ultra-shallow seismic reflection imaging in a region characterized by high source-generated noise. Near Surf. Geophys. **3**, 33–46 (2005)

R.A. Schultz, Localization of bedding-plane slip and backthrust faults above blind thrust faults: keys to wrinkle ridge structure. J. Geophys. Res. **105**, 035 (2000)

R.F. Scott, Failure. Geotechnique **37**(4), 423–466 (1987)

K.D. Seelos, F.P. Seelos, C.E. Viviano- Beck, S.L. Murchie, R.E. Arvidson, B.L. Ehlmann, A.A. Fraeman, Mineralogy of the MSL Curiosity landing site in Gale crater as observed by MRO/CRISM. Geophys. Res. Lett. **41**, 4880–4887 (2014). https://doi.org/10.1002/2014GL060310

E. Sefton-Nash, N.A. Teanby, C. Newman, R.A. Clancy, M.I. Richardson, Constraints on Mars' recent equatorial wind regimes from layered deposits and comparison with general circulation model results. Icarus **230**, 81–95 (2014)

K. Seiferlin, P. Ehrenfreund, J. Garry, K. Gunderson, E. Hütter, G. Kargl, A. Maturilli, J.P. Merrison, Simulating martian regolith in the laboratory. Planet. Space Sci. **56**(15), 2009–2025 (2008)

A. Seiff, J.E. Tillman, J.R. Murphy, J.T. Schofield, D. Crisp, J.R. Barnes, C. LaBaw, C. Mahoney, G.R. Wilson, R. Haberle, The atmosphere structure and meteorology instrument on the Mars Pathfinder lander. J. Geophys. Res. **102**, 4045–4056 (1997)

A. Shaw, R.E. Arvidson, R. Bonitz, J. Carsten, H.U. Keller, M.T. Lemmon, M.T. Mellon, M. Robinson, A. Trebi-Ollennu, Phoenix soil physical properties investigation. J. Geophys. Res. **114**, E00E05 (2009). https://doi.org/10.1029/2009JE003455

D.E. Smith et al., Mars Orbiter Laser Altimeter (MOLA): experiment summary after the first year of global mapping of Mars. J. Geophys. Res. **106**, 23,689–23,722 (2001)

P.H. Smith et al., H$_2$O at the Phoenix landing site. Science **325**, 58–61 (2009)

G.G. Sorrells, J.A. McDonald, Z.A. Der, E. Herrin, Earth motion caused by local atmospheric pressure changes. Geophys. J. R. Astron. Soc. **26**, 83–98 (1971)

A. Spiga et al., Atmospheric science with InSight. Space Sci. Rev. (2018, this issue)

T. Spohn, M. Grott et al., The Heat Flow and Physical Properties Package (HP^3) for the InSight Mission. Space Sci. Rev. (2018, this issue)

P.M. Stella, J.A. Herman, The Mars surface and solar array performance, in *35th IEEE Photovoltaic Specialists Conference*, Honolulu, 20–25 June 2010 (2010), pp. 002631–002635. https://doi.org/10.1109/PVSC.2010.5617185

J.D. Stopar, M.S. Robinson, O.S. Barnouin, A.S. McEwen, E.J. Speyerer, M.R. Henriksen, S.S. Sutton, Relative depths of simple craters and the nature of the lunar regolith. Icarus **298**, 34–48 (2017). https://doi.org/10.1016/j.icarus.2017.05.022

R. Sullivan, R. Greeley, M. Kraft, G. Wilson, M. Golombek, K. Herkenhoff, J. Murphy, P. Smith, Results of the Imager for Mars Pathfinder windsock experiment. J. Geophys. Res. **105**, 24547–24562 (2000)

R. Sullivan, R. Anderson, J. Biesiadecki, T. Bond, H. Stewart, Cohesions, friction angles, and other physical properties of Martian regolith from Mars Exploration Rover wheel trenches and wheel scuffs. J. Geophys. Res. **116**, E02006 (2011). https://doi.org/10.1029/2010JE003625

J.L. Sutton, C.B. Levoy, J.E. Tillman, Diurnal variations of the Martian surface layer meteorological parameters during the first 45 sols at two Viking Lander sites. J. Atmos. Sci. **35**, 2346–2355 (1978)

J. Sweeney, N.H. Warner, M.P. Golombek, R.L. Kirk, R.L. Fergason, A. Pivarunas, Crater degradation and surface erosion rates at the InSight landing site, western Elysium Planitia, Mars, in *47th Lunar Planet. Sci. Conf.* (2016). Abstract 1576

J. Sweeney, N.H. Warner, V. Ganti, M.P. Golombek, M.P. Lamb, R. Fergason, R. Kirk, Degradation of one-hundred-meter-scale impact craters on Mars at the InSight landing site on Mars with implications for surface process rates in the Hesperian and Amazonian. J. Geophys. Res., Planets (2018, in review)

T. Szabo, G. Domokos, J.P. Grotzinger, D.J. Jerolmack, Reconstructing the transport history of pebbles on Mars. Nat. Commun. **6**, 8366 (2015). https://doi.org/10.1038/ncomms9366

K.L. Tanaka, J.A. Skinner, J.M. Dohm, R.P. Irwin, E.J. Kolb, C.M. Fortezzo, T. Platz, G.G. Michael, T.M. Hare, Geologic Map of Mars, 1:20,000,000, USGS Scientific Investigations Map 3292 (2014)

P.A. Taylor, D.C. Catling, M. Daly, C.S. Dickinson, H.P. Gunnlaugsson, A-M. Harri, C.F. Lange, Temperature, pressure and wind instrumentation in the Phoenix meteorological package. J. Geophys. Res. **113**, E00A10 (2008). https://doi.org/10.1029/2007JE003015

N.A. Teanby, J. Stevanović, J. Wookey, N. Murdoch, J. Hurley, R. Myhill, N.E. Bowles, S.B. Calcutt, W.T. Pike, Seismic coupling of short-period wind noise through Mars' regolith for NASA's InSight lander. Space Sci. Rev. **211**, 485 (2017). https://doi.org/10.1007/s11214-016-0310-z

E. Theilig, R. Greeley, Lava flows on Mars: analysis of small surface features and comparisons with terrestrial analogs. J. Geophys. Res. **91**(B13), E193–E206 (1986). https://doi.org/10.1029/JB091iB13p0E193

N. Thomas, G. Cremonese, R. Ziethe, M. Gerber et al., The Colour and Stereo Surface Imaging System (CaSSIS) for the ExoMars Trace Gas Orbiter. Space Sci. Rev. **2017**(212), 1897–1944 (2017). https://doi.org/10.1007/s11214-017-0421-1

B.J. Thomson, P.H. Schultz, N.T. Bridges, Extracting scientific results from robotic arm support operations: a technique for estimating the density and composition of rocks on Mars. Mars **4**, 27–32 (2008). https://doi.org/10.1555/mars.2008.0003

A. Trebi-Ollennu, W. Kim, K. Ali et al., InSight Mars lander robotics instrument deployment system. Space Sci. Rev. (2018, this issue)

A.R. Vasavada, S. Piqueux, K.W. Lewis et al., Thermophysical properties along Curiosity's traverse in Gale crater, Mars, derived from the REMS ground temperature sensor. Icarus **284**, 372–386 (2017). https://doi.org/10.1016/j.icarus.2016.11.035

J. Vaucher, D. Baratoux, N. Mangold, P. Pinet, K. Kurita, M. Grégoire, The volcanic history of central Elysium Planitia: implications for martian magmatism. Icarus **204**, 418–442 (2009)

A.F. Vaughan et al., Pancam and microscopic imager observations of dust on the Spirit rover: cleaning events, spectral properties, and aggregates. Mars **5**, 129–145 (2010). https://doi.org/10.1555/mars.2010.0005

C.A. Verba, P.E. Geissler, T.N. Titus, D. Waller, Observations from the high resolution imaging science experiment (HiRISE): Martian dust devils in Gusev and Russell craters. J. Geophys. Res., Planets **115**(E9), Doi (2010). https://doi.org/10.1029/2009JE003498

C. Vrettos, Shear strength investigations for a class of extra-terrestrial analogue soils. J. Geotech. Geoenviron. Eng. **138**, 508–515 (2012)

C. Vrettos, A. Becker, K. Merz, L. Witte, Penetration tests in a mold on regolith quasi-analogues at different relative densities, in *Earth & Space 2014, 14th ASCE International Conference on Engineering, Science, Construction and Operations in Challenging Environments* (2014)

G.P.L. Walker, Structure, and origin by injection of lava under surface crust, of tumuli, "lava rises", "lava-rise pits", and "lava-inflation clefts", Hawaii. Bull. Volcanol. **53**(7), 546–558 (1991)

N.H. Warner, S. Gupta, F.J. Calef, P. Grindrod, K. Goddard, Minimum effective area for high resolution crater counting of martian terrains. Icarus **245**, 198–240 (2015). https://doi.org/10.1016/j.icarus.2014.09.024

N.H. Warner, M.P. Golombek, J. Sweeney, R. Fergason, R. Kirk, C. Schwartz, Near surface stratigraphy and regolith production in southwestern Elysium Planitia, Mars: implications for Hesperian-Amazonian terrains and the InSight lander mission. Space Sci. Rev. **211**, 147–190 (2017). https://doi.org/10.1007/s11214-017-0352-x

T.R. Watters, Wrinkle ridge assemblages on the terrestrial planets. J. Geophys. Res. **93**, 10236–10254 (1988)

W.A. Watters, L.M. Geiger, M.A. Fendrock, R. Gibson, Morphometry of small recent impact craters on Mars: size and terrain dependence, short-term modification. J. Geophys. Res., Planets **210**(2), 226–254 (2015). https://doi.org/10.1002/2014JE004630

S.G. Wells, J.C. Dohrenwend, L.D. McFadden, B.F. Turrin, K.D. Mahrer, Late Cenozoic landscape evolution on lava flow surfaces of the Cima volcanic field, Mojave Desert, California. Geol. Soc. Am. Bull. **96**, 1518–1529 (1985)

S.C. Werner, K.L. Tanaka, Redefinition of the crater-density and absolute-age boundaries for the chronostratigraphic system of Mars. Icarus **215**, 603–607 (2011)

M.A. Wieczorek et al., The crust of the Moon as seen by GRAIL. Science **339**(6120), 671–675 (2012). https://doi.org/10.1126/science.1231530

A. Wilkinson, A. DeGennaro, Digging and pushing lunar regolith: classical soil mechanics and the forces needed for excavation and traction. J. Terramech. **44**(2), 133–152 (2007)

M.M. Withers, R.C. Aster, C.J. Young, E.P. Chael, High-frequency analysis of seismic background noise as a function of wind speed and shallow depth. Bull. Seismol. Soc. Am. **86**, 1507–1515 (1996)

R.A. Yingst, A.F.C. Haldemann, K.L. Biedermann et al., Quantitative morphology of rocks at the Mars Pathfinder landing site. J. Geophys. Res. **112**, E06002 (2007). https://doi.org/10.1029/2005JE002582

R.A. Yingst, L. Crumpler, W.H. Farrand et al., Morphology and texture of particles along the Spirit rover traverse from sol 450 to sol 745. J. Geophys. Res. **113**, E12S41 (2008). https://doi.org/10.1029/2008JE003179

R.A. Yingst et al., Characteristics of pebble- and cobble-sized clasts along the Curiosity rover traverse from Bradbury Landing to Rocknest. J. Geophys. Res., Planets **118**, 2361–2380 (2013). https://doi.org/10.1002/2013JE004435